A SPIN FILTER POLARIMETER AND AN α-PARTICLE D-STATE STUDY

by

Susan Kathryn Lemieux

A dissertation submitted to the faculty of the University of North Carolina at Chapel Hill in partial fulfillment of the requirements for the degree of Doctor of Philosophy in the Department of Physics and Astronomy.

Chapel Hill

1993

Approved by :

Thomas B. Clegg, Advisor

W. J. Thompson, Reader

E. J. Ludwig, Reader

Abstract

SUSAN KATHRYN LEMIEUX. A Spin filter Polarimeter and an α-particle D-state study. (Under the direction of Dr. Thomas B. Clegg.)

A Spin Filter Polarimeter (SFP) which reveals populations of individual hyperfine states of nuclear spin-polarized $H^{\pm}$ (or $D^{\pm}$) beams has been tested. The SFP is based on unique properties of a three-level interaction in the $2S_{1/2}$ and $2P_{1/2}$ states of the hydrogen (or deuterium) atoms, created when the polarized ion beams pick up electrons in cesium vapor. The SFP has potential for an absolute accuracy of better than 1.5%, thus it could be used for calibrating polarimeters absolutely for low energy experiments for which no nuclear polarization standard exists. Test results show that the SFP provides a quick and elegant measure of the relative hyperfine state populations in the beam.

This α-particle study is a small part of a larger project studying the deuteron-deuteron configuration of the α-particle wave function (Cro93). The differential cross section and tensor analyzing powers (TAP) were measured for the $^{50}Ti(\vec{d},\alpha)^{48}Sc$ reaction to the $J^{\pi}=7^{+}$ state in ^{48}Sc at $E_x=1.097$ MeV and compared with exact finite-range distorted-wave Born approximation (DWBA) calculations. The DWBA calculations use realistic α-particle wave functions generated from variational Monte-Carlo calculations.

ACKNOWLEDGMENTS

I would like to thank

my mom, Irene Lemieux,

my dad, Robert E. Lemieux (currently residing in Heaven),

my advisor, Tom Clegg,

my committee, Hugon Karwowski,

Bill Thompson,

Ed Ludwig,

Jim Rose,

my colleagues, Jim Bowsher, Chandra Bhat,

Dave Abbott, Tom Spencer

Eric Crosson, Kurt Fletcher

Rupak Das, Tim Black

Brian Hendrix, Dennis Dinge

Zeid Ayer, Beata Kozlowski,

my "teachers" Paul Carter, Sidney Edwards,

Ken Sweeton, Al Lovette,

Bob Hogan, Pat Mulkey,

Hal Mann, UNC shop,

my daughter, Maria

and my fiance, Eric Crosson.

TABLE OF CONTENTS

LIST OF FIGURES

LIST OF TABLES

Chapter 1

Introduction

Nuclear physics began with studies of radiative emissions from radium ore in the early 1900's and continued with work by physicists studying the atom, such as Bohr and Rutherford. Atomic and nuclear physics were virtually indistinguishable at that time; researchers worked in both fields simultaneously. This thesis is a work in that tradition. The first four chapters describe the development of a polarimeter which uses the atomic physics of hydrogen beams in electromagnetic fields to deduce the nuclear polarization of a proton or deuteron beam. The last chapter is pure nuclear physics; it describes the details of a small part of a much larger study of the alpha particle.

The device assembled and tested, the spin-filter polarimeter (SFP), will provide measurements of all polarization components for proton and deuteron beams from an atomic beam polarized ion source, such as the one used presently at the Triangle Universities Nuclear Laboratory (TUNL). Often nuclear physics experiments using polarized ion beams at low energies (< 1 MeV) have had to use polarimetery information from nuclear reactions at higher energies to deduce the beam polarization. The SFP provides nuclear polarimetry for atomic beams at the source, before acceleration. Thus the polarization can be inferred for beams on target, as long as accelerating and focusing the beam do not significantly change its polarization. The polarimeter's design, its operation, and the results of the proof-of-principle experiments of this handy device are the subject of the first four chapters of this thesis.

The spin-filter polarimeter (SFP) provides a quick and elegant measure of the relative hyperfine state populations in a hydrogen (H_0) or deuterium (D_0) beam in the metastable $2S_{1/2}$ state. Since a metastable beam can be produced from the polarized H^+ or D^+ ion beam in our source, the beam polarization can be determined from this measurement. First called a Lamb-shift polarimeter (Bro71), the SFP is a variation on the Lamb-shift ion source quench-ratio technique (Ohl71). The latter has a proven accuracy of 1.5% for determining beam polarizations. The SFP has the potential for the same accuracy. It could determine absolutely the polarizations of beams emerging from our atomic beam polarized ion source (ABPIS) and it may be used to calibrate other polarimeters. It would facilitate tuning of the ion source transition unit parameters and provide routine monitoring of the beam polarization during source operation for experiments.

The expertise with the nuclear spin filter used on the Lamb-shift polarized ion source at TUNL led to the development of the spin filter technique for polarization measurements in this thesis project. The aim of the project was to prove that this polarimeter could measure the beam polarizations on the ABPIS. This goal was achieved.

1.1 The General Utility of this Technique

The SFP measures the relative populations of the nuclear magnetic substates, $m_I = \pm 1/2$ for hydrogen and $m_I = \pm 1,0$ for deuterium in H_0 and D_0 metastable $2S_{1/2}$ beams produced from polarized ion beams (H^+ and D^+) from the ABPIS. The vector, P_z, and tensor polarization, P_{zz}, can be calculated from these measurements of the relative populations, N_i , using

$$P_z = \frac{N_+ - N_-}{N_+ + N_-} \tag{1.1}$$

for protons, and

$$P_z = \frac{N_+ - N_-}{N_+ + N_0 + N_-}, \tag{1.2}$$

and

$$P_{zz} = \frac{1 - 3N_0}{N_+ + N_0 + N_-} \tag{1.3}$$

for deuterons. Therefore, the polarimeter is generally useful for all polarized beams produced with the ABPIS.

Only metastable (τ =0.14 s) $2S_{1/2}$ hydrogen or deuterium atoms with energies near 550 eV (1100 eV) for hydrogen (deuterium) can be analyzed by the SFP. The spin filter, designed at Los Alamos National Laboratory (McK68), uses a resonant 3-level interaction in the n = 2 states to separate the hyperfine components of the atomic beam. Once selected, these atoms can be "quenched" (made to decay to the ground state via the Stark effect). The relative flux "filtered" by the SFP in each magnetic hyperfine state is measured by quenching these metastable atoms downstream of the spin filter and detecting the emitted Lyman-α (λ =121 nm) radiation. Therefore, the SFP requires a metastable $2S_{1/2}$ atomic beam created from the polarized ion beam, the spin filter, and a detector of ultra-violet radiation.

This thesis describes a proof-of-principle test for the SFP, which was made on the ABPIS with an eye toward permanent installation. The source already had the systems necessary for metastable hydrogen (deuterium) beam production at 550 eV (1100 eV): an ionizer to produce positively-charged beam, and a lens system followed immediately by a cesium charge-exchange region where the metastable beam was

produced. Although the initial study, described here, was an invasive experiment, if subsequent installation of the SFP on the source were carefully planned and engineered, our results have shown (section 4.4) that it can operate on-line for all source users without interfering unduly with beam extraction.

If the SFP were mounted permanently on the ABPIS frame, it would not provide a direct measurement of the beam polarization on target. The user would also need to take care that all intermediate spin precession between the ion source and the target was correctly accomplished. A check of loss of polarization during beam acceleration and transport should be made with a well-calibrated polarimeter at the target. Once the polarization has been measured on target and the user is certain that there are no effects from beam tuning or acceleration, the SFP polarimeter could be used to monitor the beam polarization during experiments. Magnetic substate population scans could be stored in the data-taking computer after each run, providing the user with on-line polarization information.

1.2 The Atomic Beam Polarized Ion Source

The atomic beam polarized ion source produces proton ($H^{\pm}$) or deuteron ($D^{\pm}$) beams at energies from 5 to 85 keV. The ABPIS is composed of several subsystems: the atomic beam system (Din93), the ionizer system (Cle93), and the beam acceleration and focusing system, (Cle88). See figure 1.1.

The atomic-beam system consists of a dissociator, a nozzle and skimmer, two sextupole magnets, and the radio-frequency transition units. The entrant H_2 or D_2 gas is dissociated in a discharge contained in a Pyrex tube. Atoms emerging from this discharge flow through a copper nozzle, which is cooled by a helium refrigerator. The atoms have a mean internal temperature inferred to be ~5-10 K (Tho92) when they

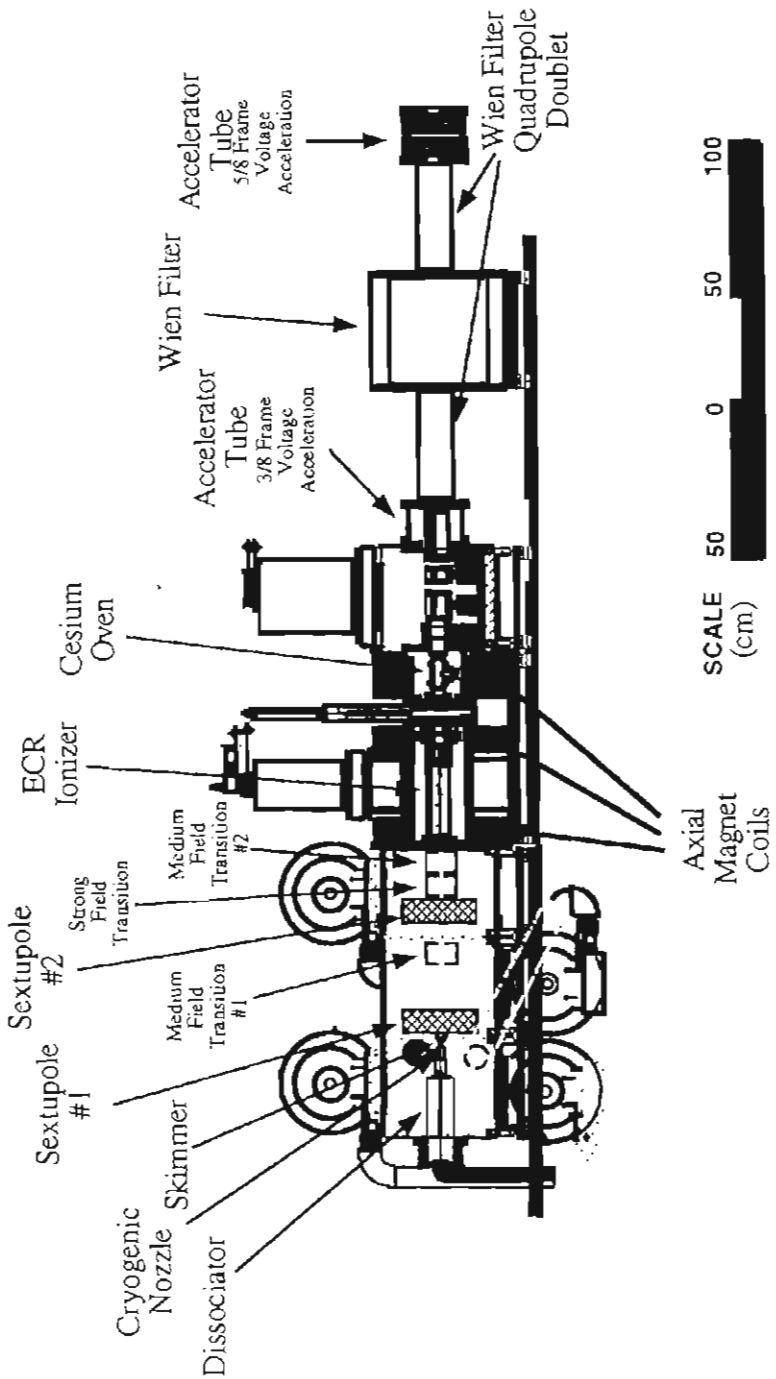

Figure 1.1 The Triangle Universities Nuclear Laboratory Atomic Beam Polarized Ion Source - A schematic diagram.

emerge from the nozzle. The atomic beam is formed when the atoms pass through a skimmer aperture located before the entrance of the first sextupole magnet.

In the field of the sextupole magnets, atoms with electron spin pointing along the axis (parallel to the direction of the local magnetic field) are focused and those with oppositely directed spin are defocused and removed. The radio-frequency (rf) transition units which produce the desired states of nuclear polarization are located after each sextupole magnet.

The ionizer system consists of an electron-cyclotron-resonance (ECR) ionizer and the cesium canal charge-exchange region. The ECR-heated plasma is confined axially and radially by magnetic fields produced respectively by solenoidal mirror coils and by a permanent magnet sextupole (Cle93). The polarized atomic beam enters the plasma, is ionized by fast-electron impact and is then extracted. This positively-charged ion beam is accelerated by a sequence of axial lenses into a cesium oven. If negative beam is desired, the cesium oven can be heated to form a cesium vapor where positive ions pick-up two electrons to make H^- or D^- ions. The ion beam is then accelerated from the source using additional axial lenses. Negatively-charged beam can be directed into either the mini-tandem (Bla93) (85-330 keV), or the tandem (1-18 MeV) accelerator systems. Positively charged beam is available for use directly from the source at 25-85 keV.

1.3 Beam Polarization Choices - the Transition Units

The radio-frequency (rf) transition units introduce nuclear polarization to the atomic beams (Din93). The nomenclature used to identify the various atomic hyperfine states for hydrogen and deuterium is that of the Breit-Rabi diagrams (Hac67). These display the energy splitting of hydrogen or deuterium atoms (cf. figure 1.2) in a magnetic field.

In the ABPIS we have a strong field (SF) rf transition unit and two medium-field transition units, MF1 and MF2. As shown in table 1.1 (Din93), certain transitions between the hyperfine states can be induced by a particular choice of frequencies and transverse magnetic fields in the units.

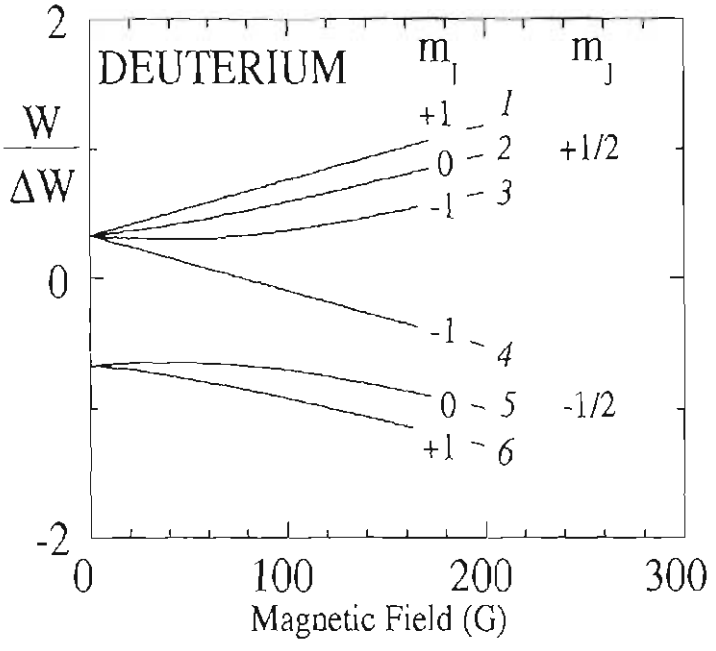

Figure 1.2 The Breit-Rabi diagram for the hyperfine splitting of deuterium atoms in a magnetic field. The y-axis is energy in units of ΔW which is defined as the zero-field separation of the quartet and doublet states.

1.4 Other Polarimeters for Low Energy Experiments

The ABPIS and new mini-tandem facility at TUNL provide polarized proton and deuteron beams of energies from 15 to 330 keV for nuclear physics experiments. Often it is important to know the absolute beam polarization, but there are few polarization standards at these low energies, especially for beams with vector polarization. There are

two ways to attack this problem. One method relies on our knowledge of the atomic physics of the hydrogen and deuterium beams; the other way utilizes known analyzing powers for previously studied nuclear reactions to determine beam polarization. Applications of these methods which have been used for low energy beam polarimetry are described below.

Table 1

Transition unit	Particle	Frequency (MHz)	B-field (mT)	Transition
MF 1	H_0	12	0.4	1->3
	D_0	12	1.2	1->4
SF	H_0	1485	16.0	2->4
	D_0	400	8.5	3->6
	D_0	460	8.0 / 16.0	2->6 / 3->5
MF2	H_0	12	0.4	1->3
	D_0	12	1.2	1->4
		28	3.6 / 3.0 / 2.5	1->2 / 2->3 / 3->4

Proton beam polarization measurement using atomic physics techniques originated with the idea (Heb60) of creating metastable $2S_{1/2}$ hydrogen beam from part of the polarized ion beam. The proposal was to remove the degeneracy of the electron spin-up and spin-down metastable atomic states with a magnetic field, quench the spin-down states, and then measure the flux of atoms in the electron spin-up states. This type of polarimeter has been built and several are currently in use (Pli76, Bel87). The SFP is a refinement of these ideas.

Another type of polarimeter measures the circular polarization of the Lyman-α radiation from a quenched metastable beam to infer the nuclear polarization of the atomic beam created from a proton beam (Cla67). This polarimeter was developed and tested for 10 to 100 keV negatively-charged hydrogen beams (Sch87).

One other atomic technique is available for a relative measure of beam polarization (Cro91). When atomic hydrogen or deuterium beams with nuclear polarization emerge from an atomic beam system and enter an ECR or electron beam ionizer, they are ionized via fast electron impact. There is a small difference, 0.01%, in the probability for ionization of a hydrogen (deuterium) atom with electron spin-up compared to the probability for ionization with electron spin-down, which arises from the spin-spin dependence of the ionization cross-section. By turning an rf transition unit off and on, and measuring the small change in beam intensity with a lock-in amplifier, the transition unit's effect on the atomic beam and the resulting proton beam polarization can both maximized. For certain transitions, the SF (3 -> 6) for example, this difference can be used to maximize the beam polarization for deuterons too. However, the technique does not provide easily a reliable quantitative measure of the beam polarization for either particle.

There are nuclear reactions which can be used for polarimetry. Once a reaction analyzing power is measured using a beam of well-known polarization, if the analyzing power is large, it can be used for effective monitoring of incident beam polarization. For protons, the $^{6}Li(p,^{3}He)\alpha$ reaction can be used to measure P_z for beams at 200-300 keV (Buc91). An effective polarimeter for deuterons can be made when A_y, A_{yy}, and A_{zz} are known for a reaction. Unfortunately, most nuclear reactions at low energies do not have both large vector and tensor analyzing powers., so most such polarimeters can be used

only in specialized applications when full knowledge of both the vector and tensor analyzing powers is not needed.

The analyzing powers A_{yy} and A_{zz} for the $D(d,p)^3H$ reaction can be used at 25-80 keV (Fle93, Tag92). These latter analyzing power measurements are reliable since they were measured using a Lamb-shift source (Tag92) from which the beam polarization was well-known. The $T(d,n)^4He$ reaction (Lis76) and $^3He(d,p)^4He$ have a known tensor analyzing power, A_{yy}, through a resonance at 107 keV in ^5He. But, A_{yy} is not well-known over a broad range of energies. For $T(d,n)^4He$ and $^3He(d,p)^4He$, A_{zz} has been measured at energies from 250 keV to 6750 keV (Dri80). None of the above reactions can provide deuteron vector polarization sensitivity.

1.5 Proof-of-principle for the SFP

As can be seen from the above discussion, a polarimeter such as the SFP which measures the polarization moments at the source for protons and deuterons could be useful. The SFP part of this thesis includes a discussion of the atomic physics of the spin filter (section 2.1), a description of the apparatus (sections 2.2, 2.3, 3.2, 3.3, 4.3), and the results of the measurements made. Measurements include the initial test on the Lamb-shift ion source test-bench (section 2.4), the installation of the SFP system on the zero-degree leg of the inflection magnet (section 3.3), and the proof-of-principle tests made on the ABPIS (section 4.4).

Chapter 2

How the Spin Filter Polarimeter Works

The spin filter polarimeter separates nuclear magnetic substates in hydrogen and deuterium atoms through a resonant interaction between three atomic energy levels. For this resonant interaction to occur, metastable $2S_{1/2}$ atoms must exist in a region with very specific electromagnetic fields, such as are supplied by the spin filter. This chapter briefly summarizes the theory of the nuclear spin filter (Ohl67, McK77, Tra74) and describes the specifics of our spin filter polarimeter system.

2.1 The Spin Filter and the Three-level Interaction

The heart of the spin-filter polarimeter (SFP) is the nuclear spin filter developed at LANL in the late 1960's. Although the mechanism for nuclear magnetic substate selection in the spin filter is based on well-understood atomic physics, it is not simple. For pedagogical purposes, a classical triple-pendulum analogy for the quantum mechanical system was developed by McKibben (McK77). This will be presented to provide some intuitive understanding of the device. Following the original work of Lamb and Retherford, McKibben and Olsen solved the atomic physics problem with a quantum mechanical treatment of the three-level interaction (Ohl67). Trainor's simplification of the quantum mechanical treatment of the three-level interaction has been used (Tra74) for calculating hyperfine state transmission through the spin filter. His approximations lead to simple equations for the transmission of the atomic states through the spin filter.

2.1.1 Hyperfine splitting and level crossings

In an external magnetic field, **B**, hydrogen and deuterium atoms with magnetic moments, μ_ε, have their energy levels split because of the interaction $\mu_\varepsilon \cdot \mathbf{B}$. Atomic states with the electron spin-up rise in energy, and the electron spin-down states decrease in energy. The levels have another smaller split due to the hyperfine interaction $\mu_\varepsilon \cdot \mu_N$. (Hae67). Notice that figure 2.1 shows this splitting for the metastable $2S_{1/2}$ state of the hydrogen atom using the nomenclature for the hyperfine states first introduced by Lamb and Retherford (Lam51).

The metastable $2S_{1/2}$ atoms have a lifetime, τ, of 1/7 s when no electromagnetic fields are present; single-photon decay from the $2S_{1/2}$ state to the $1S_{1/2}$ ground state is forbidden by electromagnetic decay selection rules. The neighboring $2P_{1/2}$ atoms have a lifetime of 1.6 ns because they can decay by an allowed electric dipole transition to the ground state. If the $2S_{1/2}$ atoms are in the presence of electromagnetic fields, their lifetimes are shortened by Stark mixing with the $2P_{1/2}$ state according to

$$\tau = \left(\frac{19}{E}\right)^2 x\ 10^{-6}\ s, \tag{2.1}$$

where E is the magnitude of the electric field in volts / cm. The quenching may arise from static electric fields or motional fields induced by passage of the atom through a magnetic field.

Deuterium atoms in the states, α_+ or β_+, with the sign designating the nuclear magnetic sub-state, will not be quenched in the spin filter static electric, static magnetic, or rf fields, if the fields are chosen such that the resonant three-state interaction occurs. Looking at figure 2.1, for a magnetic field of 565 G, the α_+, β_+, and e_+ states would

cross if there were an applied radio-frequency field near 1609 MHz such that the β_+ and e_+ levels are effectively at the same energy as the

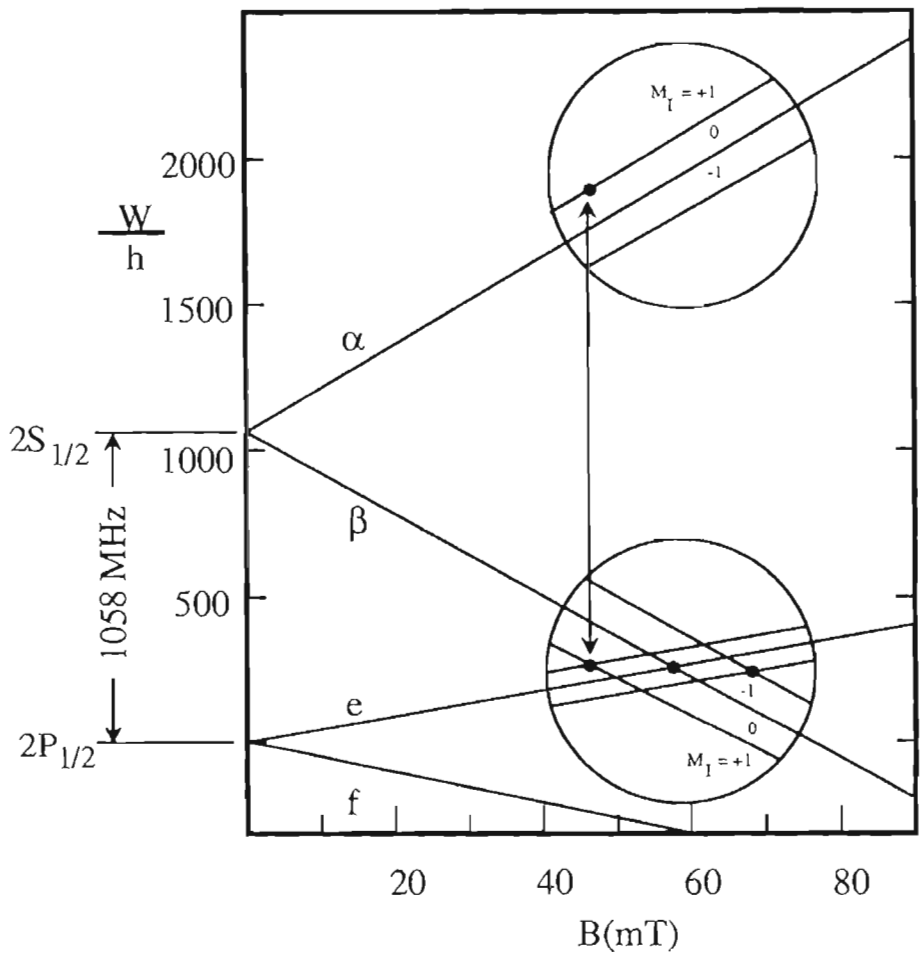

Figure 2.1 The Breit-Rabi diagram for the n=2 states of deuterium.

α_+ state. These three states are those we must consider. The argument follows identically for the α_0, β_0, and e_0 or the α_-, β_-, and e_- states. Since the physics is the same for hydrogen and deuterium atoms, from now on we will discuss the problem in terms of deuterium only - the extension for hydrogen will be implicit.

2.1.2 The Triple Pendulum Model

The three-state problem is analogous to three coupled pendula of equal mass m, see figure 2.2. The first pendulum represents the α-state and is coupled to the center pendulum, the e-state, by a spring of constant k_{12} (which characterizes the rf field). The center pendulum is coupled to the third pendulum, the β-state, by another spring of constant k_{23} (which characterizes the DC field). The springs are coupled at each end to the pendula by slip rings. Moving these rings up and down varies the strength of the coupling, equivalent to changing the strength of the electromagnetic fields in the spin filter. The static magnetic field does not explicitly appear in the equations, but the problem could not be formulated in this manner if it were not for the resonant level crossings caused by the magnetic field.

Given three pendula connected by two springs with coupling constants $R^2 = k_{12}/m$ and $V^2 = k_{23}/m$, the classical equations of motion can be written starting from the Lagrange equations. In the small oscillations approximation, using l = pendulum length, θ = angle from the vertical, ω = angular velocity, m = mass of pendulum, and g = gravitational acceleration, the Lagrangian for the triple pendulum is

$$L = \sum_{i=1}^{3} \frac{1}{2} m \ell_i^2 \omega_i^2 + \sum_{i=1}^{3} \frac{1}{2} mg \ell_i \theta_i^2 + \frac{1}{2} k_{12} (\ell_1 \theta_1 + \ell_2 \theta_2)^2 + \frac{1}{2} k_{23} (\ell_2 \theta_2 + \ell_3 \theta_3)^2 \qquad (2.2)$$

using Lagrange's equation

$$\frac{\partial L}{\partial q} - \frac{d}{dt} \frac{\partial L}{\partial q} = 0 \qquad (2.3)$$

with $q = \theta_i$, $\omega_i = \frac{d\theta_i}{dt}$, and defining the resonance frequencies by

$$\omega_1^2 = \frac{g}{\ell_1} + R^2, \quad \omega_2^2 = \frac{g}{\ell_2} + R^2 + V^2, \quad \omega_3^2 = \frac{g}{\ell_3} + V^2 \tag{2.4}$$

leads to coupled differential equations, which can be solved to determine the eigenfrequencies, ω_i , and eigenfunctions, A_i, of the system's normal modes.

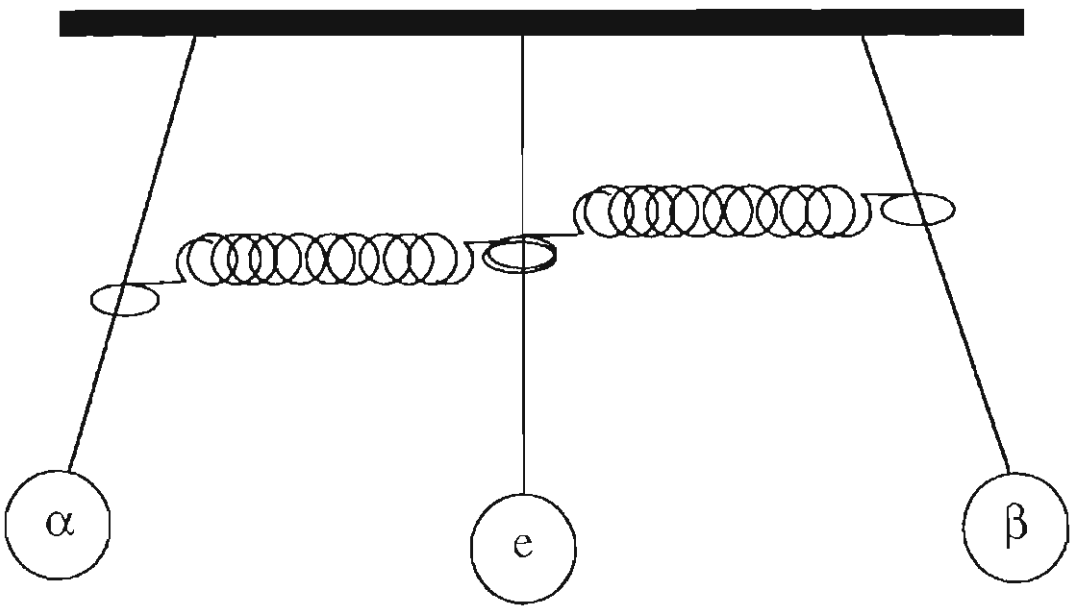

Figure 2.2 The triple pendulum - the α-e coupling spring, spring constant k_{12}, represents the rf electric field and the β-e coupling spring, spring constant k_{23}, represents the DC electric field. The pendula are of length l and the instantaneous angle from the vertical of a representative oscillator is θ.

Assuming a solution of the form $\theta(t) = \theta_0 e^{(-\gamma t)} \sin(\omega t)$ and substituting into the Lagrange equations for γ small (neglecting damping) yields

$$\begin{pmatrix} (\omega^2 - \omega_1^2) & R & 0 \\ R & (\omega^2 - \omega_2^2) & V \\ 0 & V & (\omega^2 - \omega_3^2) \end{pmatrix} \begin{pmatrix} \theta_1 \\ \theta_2 \\ \theta_3 \end{pmatrix} = \begin{pmatrix} 0 \\ 0 \\ 0 \end{pmatrix} \tag{2.5}$$

One solution of these equations is $\omega_1 = \omega_3 = \omega$, which is the mode shown in figure 2.2. This solution gives $R^2\theta_1 = -V^2\theta_3$ and $\theta_2 = 0$. In this normal mode, the middle pendulum has a null amplitude and the two outer pendula swing in opposition. This is the analogous mode to the three-level atomic resonance which preserves the α and β states (the outer pendula) - the e state (the middle pendulum) has a null amplitude. The energy splitting in the magnetic field changes so the 1609 MHz rf field couples the α and e states such that at 565 G the α_+ and β_+ states pass through the spin filter; this occurs at 575 G for α_0 and β_0, and at 585 G for α_- and β_-. For hydrogen the field strengths are 535 G for the α_+ and β_+ states and 605 G for the α_- and β_- states. The α state amplitude corresponds to $\theta_1 = -\left(V^2/R^2\right)\theta_3$. The β state amplitude corresponds to θ_3. So, the α and β states are coupled by the springs (electromagnetic fields) through the *e* state for three (two) different magnetic field strengths for deuterium (hydrogen); each corresponding to a one nuclear magnetic substate.

For a quantum-mechanical description of the system, the Schrodinger equation for a hydrogen atom in an electromagnetic field can be written as

$$i\hbar\frac{\partial\psi}{\partial t} = \mathrm{H}_0\psi + \mathrm{H}'\psi \tag{2.6}$$

where H' is the perturbation caused by the electromagnetic fields, H_0 is the Hamiltonian of the unperturbed atom, and ψ is the wave-function for the perturbed 3-state system given by

$$\psi = A_\alpha|\alpha\rangle + A_\beta|\beta\rangle + A_e|e\rangle. \tag{2.7}$$

Then using first-order perturbation theory (Sak85) and the definitions

$$\langle e|H'|\alpha\rangle = Re^{-i\omega_0 t}, \quad \langle e|H'|\beta\rangle = V, \quad \langle\beta|H'|\alpha\rangle = 0, \tag{2.8}$$

with V defined as the amplitude of the applied static electric field and R defined as the amplitude of the applied radio-frequency field, leads to the coupled equations

$$\begin{pmatrix} (\omega+\omega_0)-\omega_\alpha & R & 0 \\ R & \omega-\omega_e & V \\ 0 & V & \omega-\omega_\beta \end{pmatrix}\begin{pmatrix} A_\alpha \\ A_e \\ A_\beta \end{pmatrix} = \begin{pmatrix} 0 \\ 0 \\ 0 \end{pmatrix} \tag{2.9}$$

Since the energies of the e and β states are degenerate at the resonant value of the magnetic field, there are only two energies (frequencies) in the problem, $\omega_\beta = \omega_e = \omega$ and $\omega' = \omega_0 + \omega$, where $\omega_0 = 1609$ MHz is the applied rf frequency. Then, as in the case for the triple-pendulum, the α and β states are coupled through the e state, which

has a null amplitude, and only the atoms in one nuclear magnetic substate, in the α_i or β_i state, will not be quenched in the spin filter. Again, since the resonant interaction occurs when the α state is 1609 MHz above the β–e level crossing, only α_+ deuterium (or hydrogen) nucleus spin-up atoms emerge when the magnetic field is at 565 G (or 535 G), whereas only α_- deuterium (or hydrogen) nucleus spin-down atoms emerge at 585 G (or 605 G) and only α_0 deuterium nucleus spin-along) atoms emerge when the magnetic field is 575 G.

This argument presents a simplistic picture of a complicated three-state interaction. The approximations used for this analogy are only valid at the β–e crossover. For a more complete treatment of the problem, in order of increasing complexity, the reader is encouraged to peruse McKibben (McK77), Trainor (Tra74), Ohlson (Ohl67) and Lamb (Lam52).

2.1.3 The Transmission Function

The behavior of the metastable hydrogen atoms in the spin filter is described by a set of three coupled equations, as was seen in section 2.1.2 . These equations can be solved numerically, but with some approximations analytical solutions are possible (Tra74). Using these analytical solutions, expressions for the lifetimes of the α, β, and e states can be derived.

From the lifetimes, an expression for the transmission function for the α, β and e states can be derived. The transmission function can be thought of as a "preservation" quantity. It describes the fractional population atoms in the α, β, or e state which survive transversal of the spin filter as a function of spin filter fields. In the region near the β -e crossover Trainor (Tra74) showed that

$$T_{3L} = \exp\left\{ \frac{t(R/2)^2 \gamma\delta}{\left[\left(V^2 + (R/2)^2 - \delta(\delta + \omega_{\beta e})\right)^2 + (\delta\gamma/2)^2\right]^2} \right\} \qquad (2.10)$$

with t the time, V and R the dc and rf coupling field strengths respectively, γ the reciprocal lifetime of the $2P_{1/2}$ state, and $\delta = \omega_{\alpha\beta} - \omega$ the energy offset from the β-e crossover value. The subscript 3L denotes the three-level approximation used by Trainor to drive this quantity. The transmission function in the three-level approximation corresponds to transmission for the α state near the β-e cross-over. It is sharply peaked versus magnetic field with a maximum near the β-e crossover. The shape versus B is roughly Gaussian with a width determined by the specific relationship of the magnitudes of the DC and rf electric fields. The width of the transmission function peak is given roughly as

$$W = \frac{V^2 + \left(R/2\right)^2}{\left(R/2\right)}. \qquad (2.11)$$

The width is important for the deuterium state separation since the peaks are only 10 G apart. Increasing the DC electric field will broaden the peaks and increasing the rf power will narrow them. Thus, the three-level approximation provides a simple and illustrative expression for the α-state transmission and the associated width versus magnetic field.

In summary, a device built with a combination of a static magnetic longitudinal field, a transverse magnetic and longitudinal electric rf field, and a static transverse electric field can use the triple-state interaction in the hydrogen and deuterium atom to separate the nuclear magnetic substates of an atomic beam. Such a device has been built

and it is called the nuclear spin filter. The above discussion sketches the theory to provide some physical insight into the workings of the spin filter. The reader is encouraged to explore the original reference material to gain further understanding of this elegant device.

2.1.4 The Lamb-shift polarized ion source

The polarized ion source used at TUNL before the ABPIS was of the Lamb-shift design (Cle74). These sources are well-known and have been widely used although there are fundamental limits to their maximum output beam current (Ben89). Their primary advantages are the quench-ratio technique (Ohl71) to measure the beam polarization and the ease of obtaining nuclear-polarized beam using the spin filter (McK68).

A Lamb-shift polarized ion source (LSPIS) requires: a source of positive ions; a cesium charge-exchange region to produce metastable $2S_{1/2}$ atoms; a spin filter or related technique to produce nuclear polarized atomic beam; and selective ionization in argon gas for these polarized atoms to provide negative ion beams that can be accelerated, focused, and analyzed.

The spin filter produces nuclear-spin-polarized atomic beam if the appropriate resonant value of magnetic field is chosen (535 G and 605 G for protons with $m_I = +1/2$ and $-1/2$, respectively; 565 G, 575 G, and 585 G for deuterons with $m_I = +1, 0, \text{and} -1$, respectively) as explained above. A beam of given polarization from a Lamb-shift ion source is produced by using the spin filter at one of the above values of the magnetic field.

The "quench ratio" method for measuring beam polarization (Ohl71) consists of measuring the normal output current from the source, I, then measuring the background

beam current, I_b , when all of the metastable $2S_{1/2}$ atoms have been quenched to the ground state before their entry into the spin filter. The beam polarization is given by

$$P_b = {}^{(I - I_b)}\!/_{I} \tag{2.11}$$

assuming that the background is completely unpolarized and that the spin filter is 100% efficient at selecting states. The absolute accuracy of this method has been shown to be 1.5% or better (Ohl71).

Results from LSPIS used at TUNL, LANL, and the University of Munich (Sch87) indicate that in routine operation, usefully high beam polarization and respectable beam currents are attained. Because the performance of the Lamb-shift type sources is not as good as the more modern atomic beam sources, development and use of Lamb-shift sources has declined.

2.1.5 The spin filter as a polarimeter

The spin filter can be used as a polarimeter (Bro71) for a beam of $2S_{1/2}$ atoms by varying the magnetic field through the resonant values and counting the atoms of each nuclear magnetic spin projection which pass through the spin filter. Thus a measurement of the relative populations of the hyperfine states can be made.

Following the spin filter, the emerging metastable atoms in the "filtered" hyperfine state can be quenched and the Lyman-α photons detected. Sending the signal from the photon detector to an ADC in synchronization with the spin filter magnetic field can generate "polarization spectra" in the computer.

Peaks, seen in figure 2.3, of equal size show that the incident metastable beam is unpolarized. Clear evidence for vector or tensor polarization appears when a magnetic

field scan shows significantly different nuclear magnetic substate populations and values for both P_z and P_{zz} can be calculated very easily.

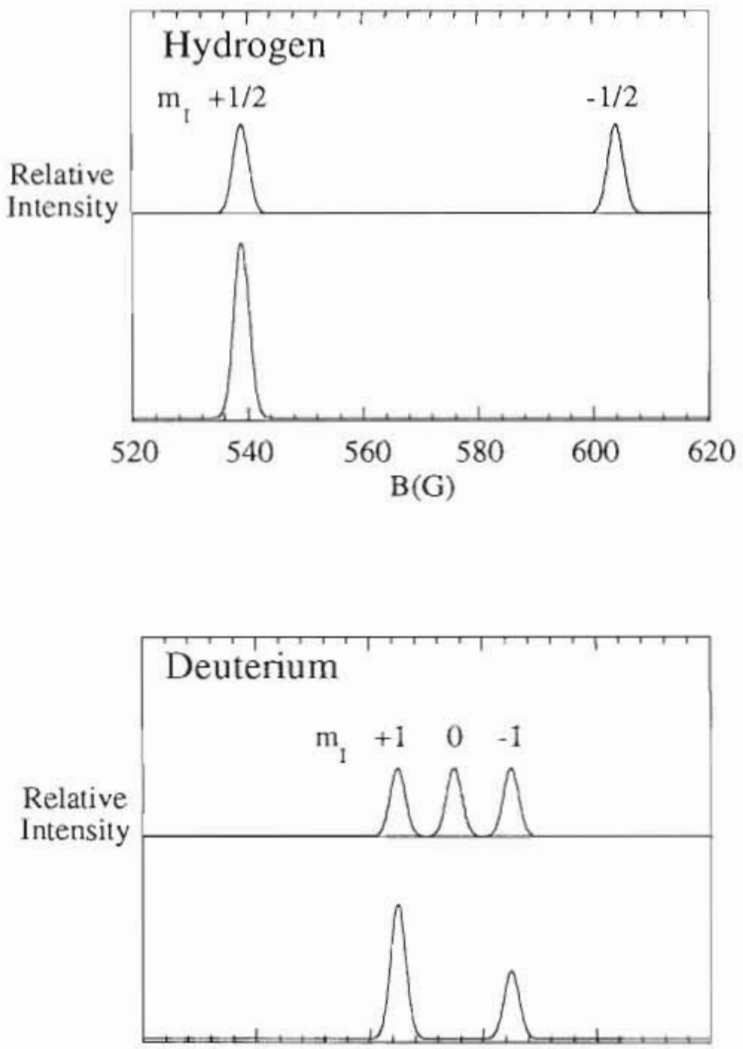

Figure 2.3 Idealized scans for hydrogen and deuterium. The top panels show unpolarized scans with exactly equal peak areas and heights. The bottom panels show scans for 100% polarized beams, for hydrogen P_z=+1 and for deuterium P_z=+1/3, P_{zz}=+1.

2.2 Metastable atom detectors on the Lamb-shift source test bench

The Lamb-shift ion polarized ion source (LSPIS) was decommissioned at TUNL when the ABPIS came on-line in 1989. Thus it became available for use as a test bench for the SFP, (see figure 2.4). In this capacity the LSPIS served two purposes. We tested several Lyman-α photon detection schemes. We demonstrated successful operation of a physically shorter, previously unused, spin filter system before installation on the ABPIS.

The Lamb-shift ion source was blanked-off at the downstream end and moved away from the tandem accelerator so that it became a stand-alone system with its own power, water, air and oil lines. Also, its argon coil was removed, since negative ion production was unnecessary. This left the Lamb-shift source as a three-component system: a duoplasmatron for the positive ion production; a cesium oven and deflection plates for production of $2S_{1/2}$ metastable atomic beam; and a spin filter and detector.

During test runs, positive ion currents of ~1mA emerged from the LSPIS duoplasmatron to enter a cesium oven canal where ~30% of the 550 eV (1100eV) hydrogen (deuterium) ions could be expected to form $2S_{1/2}$ metastable atoms (Cle84). Next, the atoms passed between a pair of oppositely-biased deflection plates which could be biased from 0 to ±300 V. When the deflection plates were slightly biased to ±5-30 V, they swept aside the charged particle beam, leaving a core of atomic beam which entered the spin filter. When biased to higher voltages, ± 100-300 V, these plates quenched the metastable beam thus providing a valuable check for background signals in the metastable-atom detector. Any signal present with the deflection plates biased to 200 V

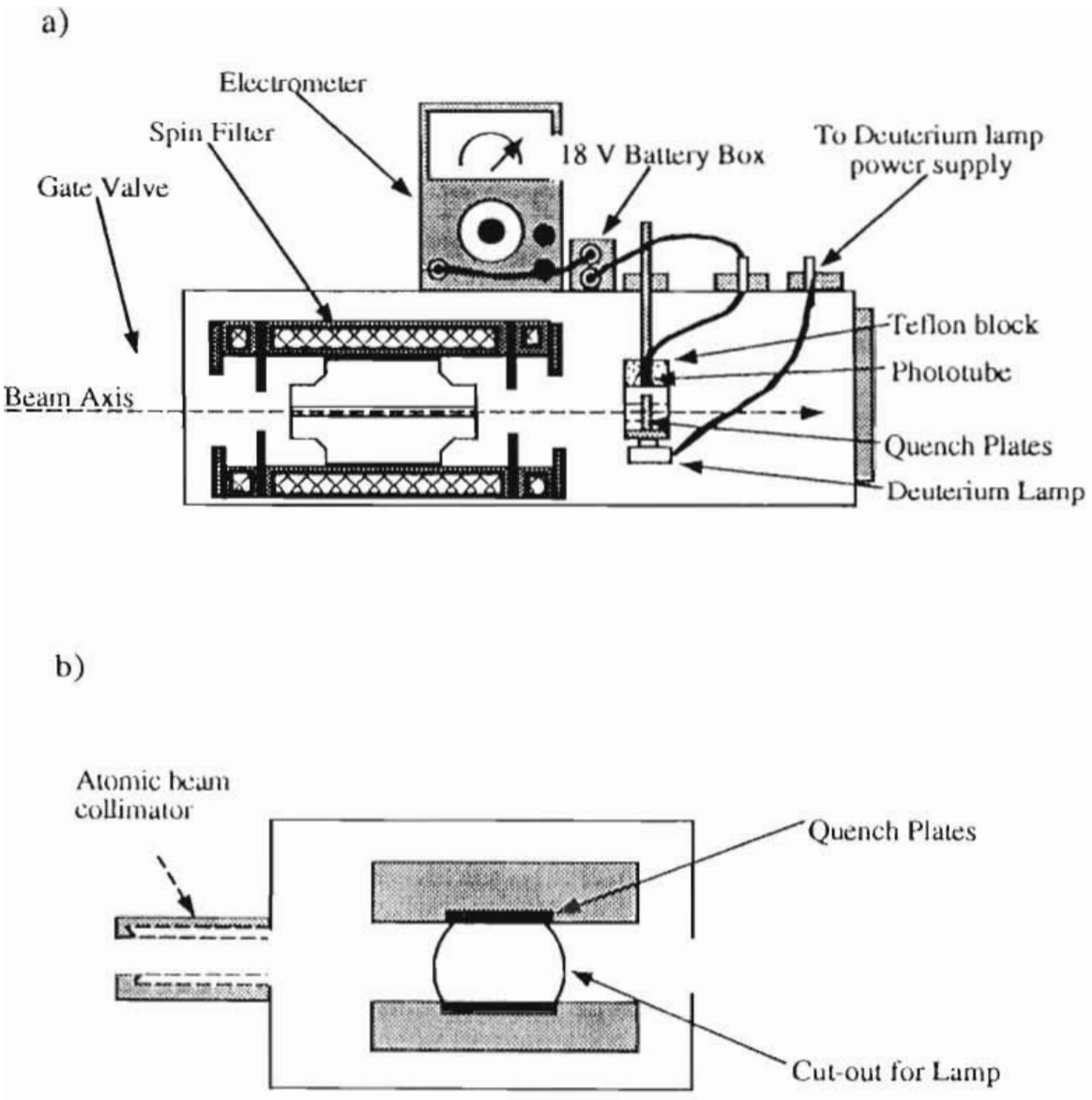

Figure 2.4 a) Lamb-shift source test bench. b) Detector box as seen by the phototube.

had to be background, since metastable atoms would decay to the ground state in that electric field.

After the deflection plates, the metastable beam passed through the spin filter. The detector was placed on-axis at the exit of the spin filter. The detector alignment on-axis was accomplished by shining a laser through the 0.5 mm diameter duoplasmatron anode aperture and onto crosshairs mounted on the spin filter entrance and on the detector holder entrance.

The detector holder had previously been used in an earlier measurement of the Lyman-α photons made by S. Mitchell (Cle82). The holder was a small box of dimensions 5 cm x 7.5 cm x 7.5 cm which contained 1 cm x 1 cm quench plates and an insulating block for mounting the detector, see figure 2.4. A collimator was mounted on the front face of the box to reduce scattering of the beam into the detector, and an exit aperture was provided for the same reason. The box was attached to a rod inserted through a sliding seal on the top of the source vacuum chamber. The whole assembly was grounded to eliminate small background currents caused by the beam. Inside, one quench plate was biased to 100V and the other plate, 1 cm away on the opposite side of the beam, was grounded. The detector viewed the quenching region between these plates from its mounting block above the plates at a distance of 2.5 cm.

Lyman-α radiation can be detected by a variety of detectors currently available. On the Lamb-shift ion source test bench, we tried two different types, See also section 3.1 for descriptions of other detectors considered later. We could expect a high flux of photons under these test conditions on the LSPIS and later on the ABPIS, so gain was not a major consideration. We wanted a detector which would be sensitive to a small bandwidth about the 121nm wavelength. Also, the detector must be insensitive to electromagnetic fields and to electronic noise from the beam or vacuum pumps.

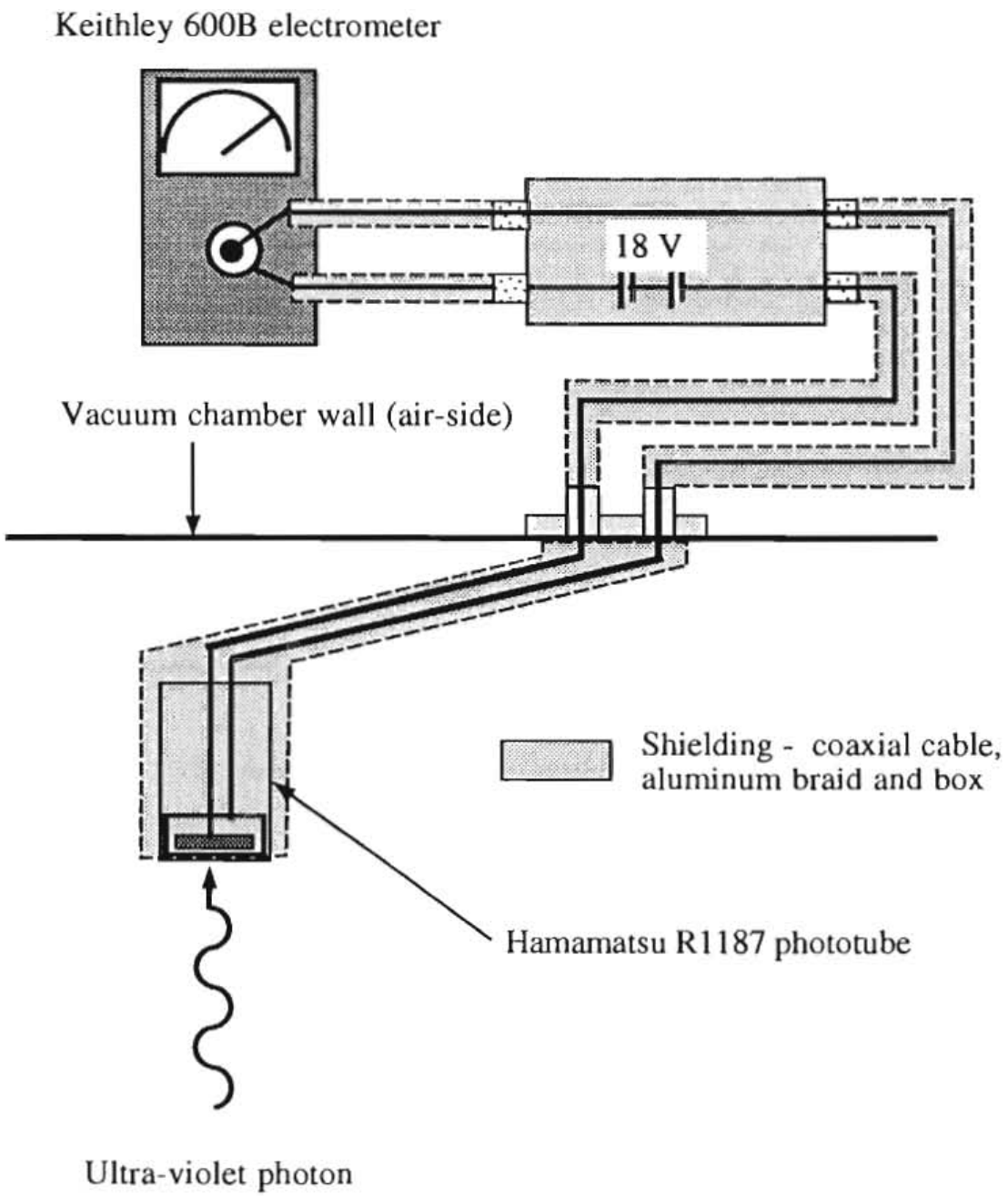

Figure 2.5 Electrical connections for Lyman-α photon detection on the LSPIS test bench.

The first detector tested was a vacuum ultraviolet photo-ionization chamber available from Artech Corp, the type used by Mitchell. This is an ionization chamber filled with NO gas with a MgF_2 entrance window which could be operated in either unity or high gain mode depending on the applied voltage. The NO gas ionization potential determined the low energy (long wavelength) cutoff at 134nm and the MgF_2 window determined the high energy (short wavelength) cutoff at 112 nm. This detector has a high quantum efficiency, up to 60%, for detecting ultraviolet radiation, and the bandpass is narrow, which would discriminate against background light. However, it has two major disadvantages. The NO gas is dissociated by the detected photons neccessitating occasional replacement or refilling of the detector, and NO gas is a Class A poison - the detector must be handled with caution.

Fortunately, another small detector was available. The detector that we used on the test-bench and that we are using now as a metastable detector in the ABPIS (see section 3.2) is a Hamamatsu Model R1187 phototube. Photons incident on these phototubes generate electrons via the photoelectric effect on a disk-shaped CsI cathode. The electrons are attracted to a cylindrical anode which surrounds the cathode; the resulting current can be measured on an electrometer. The detector has a long wavelength cutoff at 200nm determined by the work function of the CsI and a low wavelength cutoff determined by the transmission of the MgF_2 window, as in the NO detector. Figure 2.6 displays the quantum efficiency versus wavelength for the R2050 photomultiplier tube with a CsI cathode and an MgF_2 window. The R1187 has a quantum efficiency of 10% at 121 nm. The quantum efficiency dependence on wavelength has the same shape for both the R1187 and the R2050 which is characteristic of the CsI cathode and MgF_2 window.

The signal was expected to be quite large, assuming 1 mA of H^+ or D^+ from the duoplasmatron, roughly 30% of which could be expected to emerge from the cesium oven as metastable 2S beam. After considering the losses from solid angle and collimation, we expected a signal of roughly 10 pA. Mitchell had seen signals

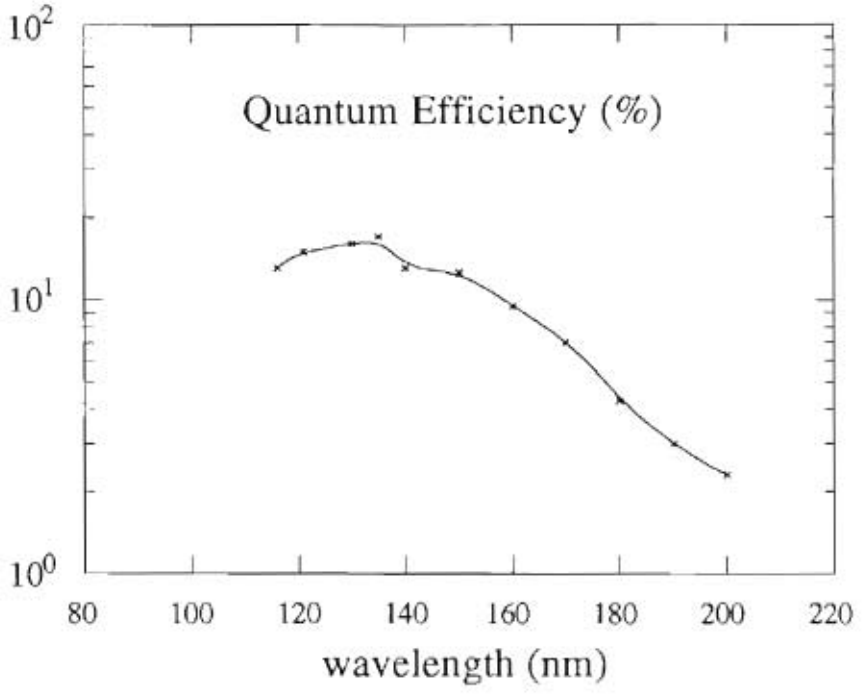

Figure 2.6 The quantum efficiency for the R2050 photomultiplier tube. These data were supplied by Hamamatsu with the R2050 tube that was purchased for the SFP.

of 10-100 pA. The current from the detectors was read on a Keithley Model 600B electrometer capable of measuring signals as small as 0.1 pA.

The primary obstacle to measuring small electric currents are other currents caused by the beam. The beam strikes an object, for example the detector box, and if the path of

least resistance is through the electrometer circuit, then a "background" current will be measured. If there is a resistance of 1000MΩ and a potential difference caused by the charging of a surface by the beam of 1mV then a 1pA signal will be detected. Therefore, all the wiring for the detector had to be well-shielded and that shield had to be well-grounded. Capacitive pick-up by the wiring external to the vacuum chamber was another problem which was partially resolved by placing the electrometer close to the vacuum feedthrus for the detector and shielding those wires as well. The circuitry is shown in figure 2.5 .

The first detector used was the NO ionization chamber, but the NO gas was depleted during the first tests while we solved the shielding problems. Rather than face the stringent safety requirements for the handling and storage of NO gas, we subsequently used the above-mentioned Hamamatsu Model R1187 phototube.

While testing the new phototubes, we developed a technique for testing the electrical circuitry without beam. The capability for conducting off-line tests is very important, because using a beam to test the detectors introduces many complications: noise from scattered electrons and beam particles, questions about metastable beam production and background light from the duoplasmatron, worries about connections, etc. Deuterium lamps were procured that emitted within the phototube's range of spectral sensitivity. The simplest test was to connect the detector in situ and shine a lamp on its active surface.

The deuterium lamps used were bulbs made by Mitsubishi for mass-spectrometer systems. The lamps emit a continuous spectrum of radiation from 185 to 400nm, beyond the 121 nm wavelength of Lyman-α photons but within the sensitive spectral range of the phototube . These lamps emit visible light of a bright lavender-purple as well as ultra-violet light, and so they should not be looked at directly. The lamp intensity can be adjusted by raising or lowering the lamp DC voltage. Currents on the electrometer

while the lamp was shone on the detector face measured from 30 pA to 800 nA. The lamps we used emitted unreliably and had been removed from earlier mass spectrometer use for that reason, but they were adequate for our purpose. Deuterium lamps are also available from Hamamtsu.

The deuterium lamp was mounted under the detector box so that it shone directly into the detector, as shown in figure 2.4. The lamp was controlled by a power supply external to the vacuum chamber so the detector could be tested with the lamp without breaking vacuum.

So, with a working detector mounted after the spin filter, we were ready to look for hyperfine state separation using the spin filter on the test bench. The first tests used the longer spin filter which was previously part of the Lamb-shift source. These tests were successful because when we scanned the magnetic field in the spin filter through the resonant region we observed the three peaks in the current attributable to the three deuterium hyperfine states. The peak currents were 10 pA on a flat background of 2-3 pA.

The longer spin filter magnet system could not be used for the SFP, because of details of its construction. A second shorter spin filter system of appropriate design was available for the polarimeter project, but this shorter spin filter had to be refurbished and tested.

2.3 The Spin Filter Magnetic-field Requirements

The spin filter polarimeter requires a highly uniform static magnetic field, a radio-frequency field, and a static electric field for its operation. The spin filter magnet system was originally designed at LANL by Ohlsen and McKibben (Ohl69 -1) and a similar

system was built in a slightly modified form at TUNL by Clegg. This magnet system has six solenoidal coils to provide the static magnetic field. Inside the coils is placed the four-segment rf cavity which provides the time-varying and static electric fields (Ohl69-2). This section is a discussion of the static magnetic field.

The six coils used were: one main coil, two trim coils, two end coils, and an inner coil. These are contained in an iron "can" and are cooled by transformer oil circulated through the can. The can is also vacuum tight to 2×10^{-6} torr. There are two plates of Armco iron, one at each end of the main coil, for field-shaping and flux return.

The main coil operated at 9-12 A, 30-45 V, generating heat which was conducted away by the continuously pumped oil bath. Oil flowed in through 1/4" copper tubing, entering at the bottom on one end of the spin filter and exiting at the top of the other end, an arrangement which ensured that the can was always full of oil. An oil pressure sensor ensured that the pump was always operating when the coils were energized. The coil power supplies were interlocked with this sensor to protect the coils from overheating.

The presence of the Armco iron plates changes the slope of the axial magnetic field appreciably from that expected without them. The easiest way to understand the contributions made by individual coils was to make measurements with the main coil energized, then to turn the coil of interest on then off. The difference in those measurements was then plotted as in figure 2.7a. Knowing the position of each coil's maximal effect helped determine what coil currents were needed for best field uniformity.

The magnetic field is required to be flat over the central region of the rf cavity inside the spin filter. The LANL group achieved field homogeneity of ± 0.2 G at 600G over a 25 cm length (Ohl69-1). Our experience indicates that this requirement can be relaxed to at least ± 0.3 G at 585 G over a length of 15.5 cm. On two separate occasions, clean hyperfine state separation was achieved for deuterium operation although magnetic field

measurements made later indicated uniformity of only the ± 0.5 G. Although the LANL requirement may be too strict, we always adjusted the coil currents for the best field uniformity attainable. All field measurements were made using a ruled jig which positioned a Hall probe exactly on-axis. Anticipating a permanent installation on the ABPIS, where field adjustments would be difficult, all measurements were checked repeatedly for reproducibility.

Reproducible and reliable measurements were made when the spin filter coils had been energized for several hours before the measurements. On repeated occasions, however, the field uniformity over the required 15.5 cm region would degrade from ± 0.15G to ±0.5G overnight. After re-establishing field uniformity, measurements made 24 hours later retained the ± 0.15G uniformity. It is possible that such a large piece of iron takes a long time to reach its final thermal equilibrium, and therefore extensive time at full current was required to obtain the final coil resistance. The best reproducibility was attained when the coils had been energized for at least 24 hours.

The inner coil was used to scan the magnetic field through the resonant region from 520-620G. It was energized by a programmable Kepco Bipolar Operational power supply which could be operated remotely to scan the resonant region at frequencies up to 1Hz. Scans at higher frequencies are not possible because of the large mutual inductance between the main coil and the inner coil. The field homogeneity was checked with the inner coil energized. It had no effect on the overall flatness of the magnetic field. Figure 2.7b displays the shape of the spin-filter axial magnetic field with all of the coils energized.

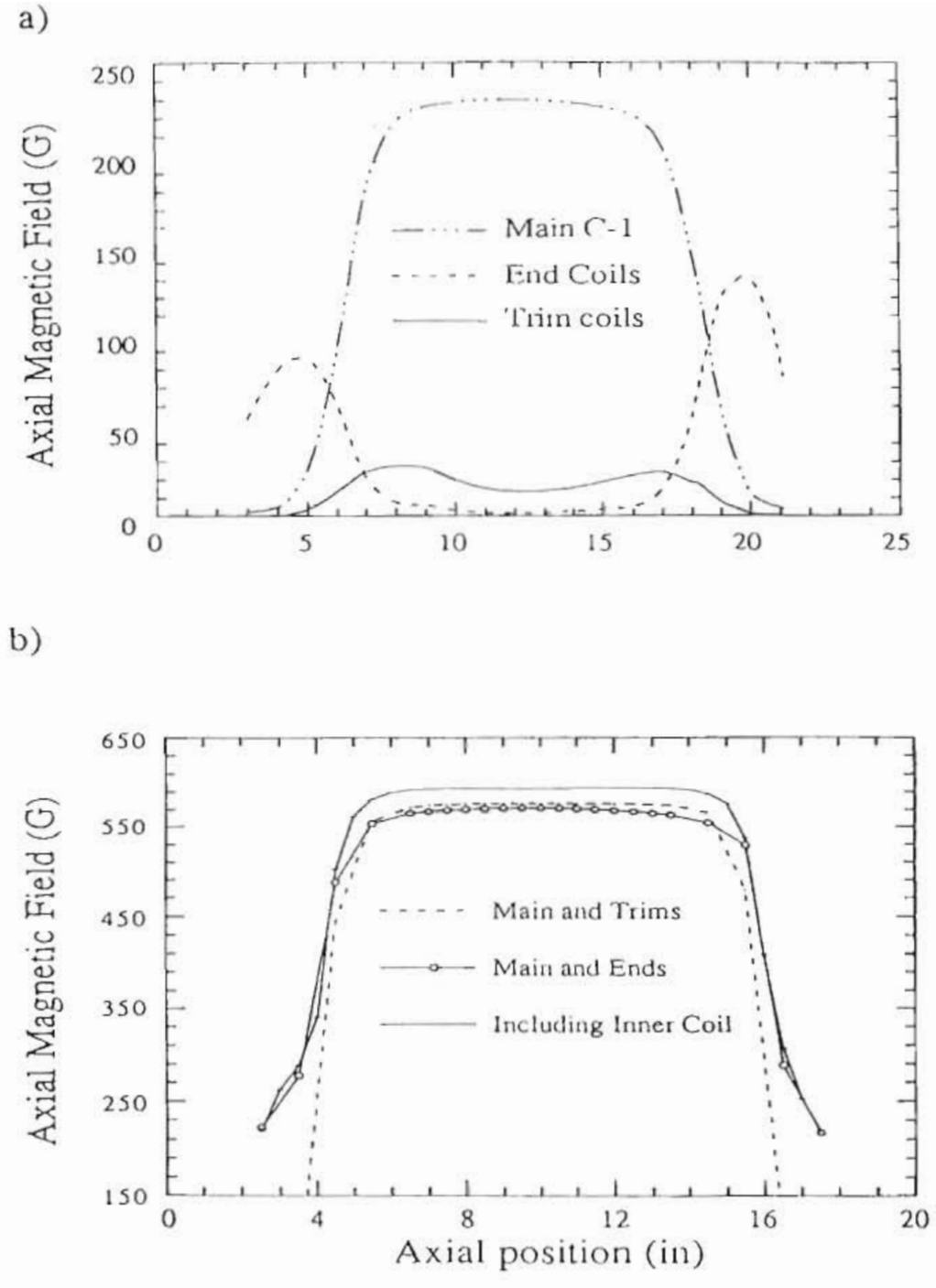

Figure 2.7 a) The individual contributions to the axial spin-filter magnetic field. b) The axial magnetic field in the spin filter with combinations of coils energized. The solid line, labelled "including inner coil" is a typical measurement, flat to 0.4 G.

2.4 The Spin Filter Radio-frequency Cavity

The triple-state interaction requires the uniform static magnetic field, a static transverse electric field and a radio-frequency longitudinal electric field as discussed in section 2.1. The static magnetic field has been described in section 2.2. This section is devoted to a discussion of the rf and dc electric fields in the spin filter.

The radio-frequency (rf) field at 1609 MHz was provided by a cylindrical copper cavity with "end pipes" . A full description of the cavity design is given in a Los Alamos National Laboratory report by Ohlson (Ohl69-2). The cavity has four longitudinal quadrants which are electrically isolated from each other. This feature allows the user to bias two of the

sides to opposite voltages $\pm V$ providing the static transverse electric field. The other two quadrants have feedthroughs for the drive and pick-up loops for the rf power.

Although the radio-frequency cavity had already been designed and constructed, it had not been tuned for 1609 MHz. The tuning of the rf cavity required several procedures: an adjustment of the cavity's geometry, a measurement of the loaded Q-value, impedance matching of the drive and pick-up loops with the cavity, and calibration for the feedback loop and power level.

The mode supported in the cavity is the TM_{010} mode which has only longitudinal electric fields and azimuthal magnetic fields. (The cavity design, with the length and diameter equal, has another mode, TE_{111}, which is degenerate with the TM_{010} mode. The TE mode is suppressed by the longitudinal cuts which inhibit the surface currents in that mode.)

The cavity's diameter could be adjusted by screws at each end used as "pushers" and "pullers". An oscillator of adjustable frequency was used with a spectroscopic amplifier

while adjusting the cavity geometry to support the desired TM_{010} mode at 1609 MHz. This part of the rf tuning was simple and straight-forward.

The load on the rf circuit changes depending on the beam current entering the cavity, the chamber pressure, and the temperature. To stabilize the power input to the cavity, a feedback circuit using a crystal detector and a PIN modulator had been designed for the previous spin filter, see the circuit diagram in figure 2.8 .

Once the tuning had been completed with the rf cavity on the bench, the spin filter was re-assembled and remounted in the LSPIS. The crystal detector voltage output was sent to an oscilloscope and the 1609 MHz rf generator was replaced with the variable oscillator so the cavity frequency and the Q could be checked. The Q was roughly 4000. The oil cooling pump was started, the coils were energized , and after 12 hours the resonant frequency was measured. It had drifted from 1609.0 to 1609.5 MHz.

We discovered that the thermal expansion of the rf cavity as it was heated by the coils caused this frequency shift. The calculated temperature coefficient of the cavity resonance frequency is -26 kHz /^{o}C. Therefore, with the full-width at half-maximum of 380 kHz, a 7^{o}C change in the cavity temperature would move the frequency to the half-power points of the cavity resonance. Since the cavity could not be tuned while installed within the spin filter, we had to lower the Q to stay on resonance.

The rf cavity from the previous spin filter was removed for comparison. Its Q was 2700 and its resonant frequency was 1608.6 MHz. The drive and pick-up loops and cables from the previous cavity were then connected to the SFP cavity so a direct comparison could be made. The Q was 4400 and the frequency was 1608.1 MHz. The impedance match was excellent for both cavities using the older loops and cables. Forward power of 160 mW with no reverse power was measured. We decided to leave the older loops on the cavity for the SFP spin filter. This lead to a lower Q of 1600,

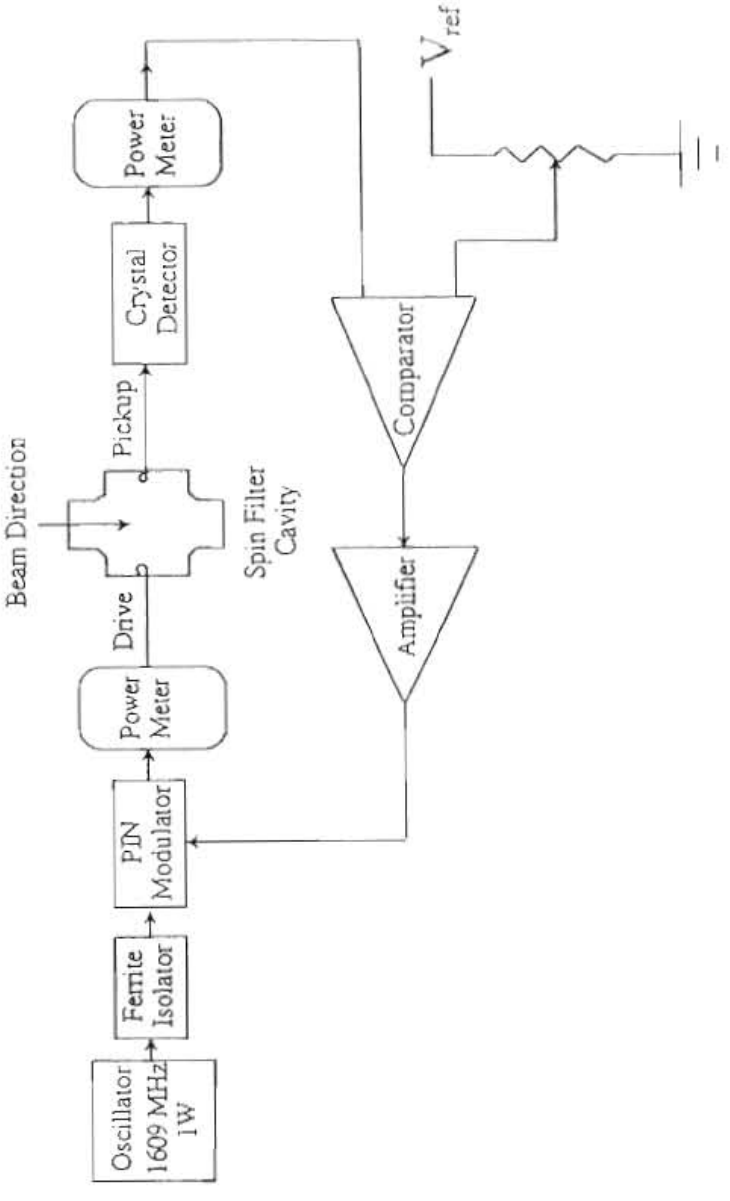

Figure 2.8 Block diagram for the radio-frequency circuit in the SFP.

which would solve the expansion problem, and still gave a good impedance match. The SFP spin filter was reassembled and installed in the LSPIS. We were ready to look for the peaks.

2.5 Test-bench Results for Hydrogen and Deuterium Atoms

The first attempt to measure the state separation on the LSPIS test bench with the SFP spin filter, the Mitchell Lyman-α detector box, and the phototube was satisfyingly successful. The three spin states for deuterium were cleanly separated and the peaks for hydrogen were seen as well. The background signal was 2pA and the peak signal was 8 pA for deuterium. For hydrogen the background was 0.4pA and the peak signal was 2 pA. So, the signal-to-noise ratio was not very high, $S/N = 4$.

We tried several different collimation schemes to improve the signal to noise ratio. The best results were obtained when we removed the detector box completely, giving a peak signal of 15 pA and a background of 4 pA.

At this point we decided that nothing more was to be gained by continued tests on the LSPIS test bench. We had tested the SFP spin filter and gained some expertise in ultraviolet photon detection. We began to prepare for tests using the beam from the ABPIS.

Chapter 3

Zero-degree Beamline Measurements

The first tests of the SFP were made downstream of the ABPIS on a "zero-degree beamline" especially constructed for these experiments, (see figure 3.1). Our hope was that the SFP could be installed without interfering with the routine use of the ABPIS. Although the test results taught us that the SFP could not be used on the zero-degree beamline, it did serve as a second, more rigorous test bench and we learned a lot about the SFP's operation and ABPIS metastable beam production.

The SFP had to be assembled as a stand-alone system and tested with ABPIS metastable atomic beam, an essential step in preparing for installation on the ABPIS. Source parameters for maximum metastable beam production could then be determined without affecting the source availability for other users. Also, there was a chance that the polarimeter would be usable on the zero-degree beamline for polarization "tuning" and would not be installed on the ABPIS in that case.

The zero-degree beamline was built from the zero-degree port on the ABPIS inflection magnet. The magnet is usually used to analyze the ABPIS beam and steer it into either the tandem accelerator or the LEBF beamline. But, since atomic beam cannot be electrically or magnetically steered, the metastable atomic beam drifted downstream through the inflection magnet then into the spin-filter polarimeter.

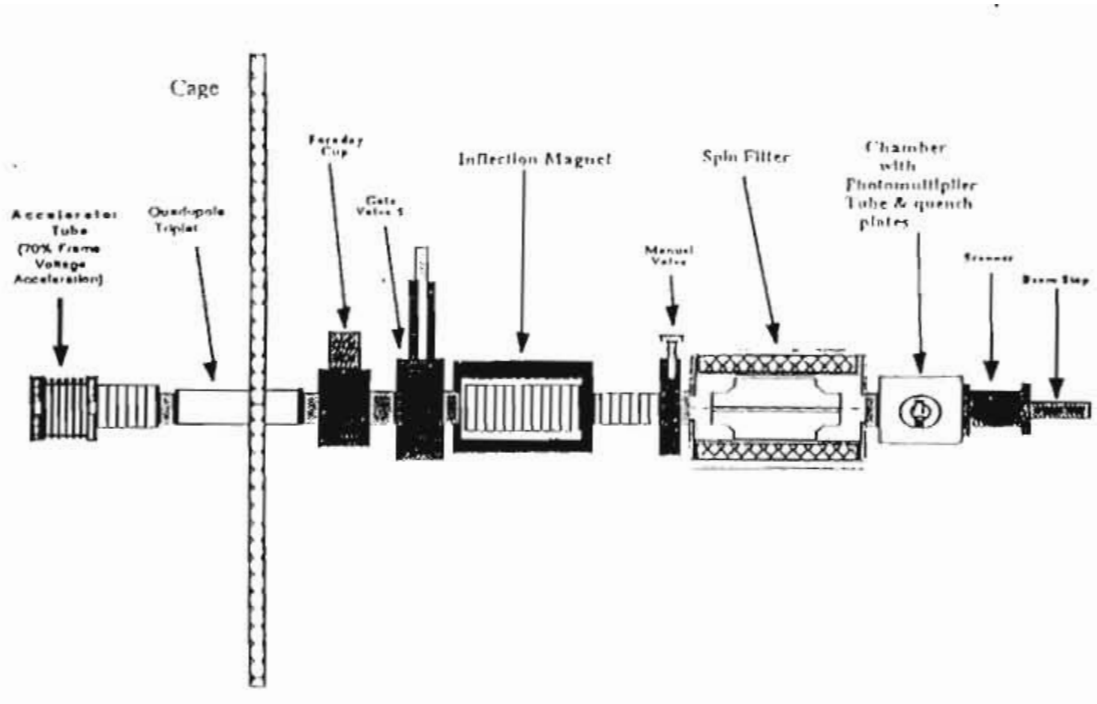

Figure 3.1 The zero-degree spin-filter polarimeter beamline

There were, however, many uncertainties associated with the zero-degree installation. The metastable beam had to drift four meters to reach the detector, therefore the atomic beam flux would be significantly reduced by the beam divergence. Also, the delicate metastable beam would have to drift without encountering any significant electric fields, static or motional, since these would quench the metastable atoms.

The tests were very useful since we completed much of the work necessary to prepare for the final proof-of-principle test with the SFP mounted on the ABPIS. The following chapter discusses this development work and the results obtained.

3.1 Design and Construction of the Zero-degree SFP Beamline

Many tasks had to be completed to prepare the zero-degree apparatus for an experiment with the ABPIS beam. A more suitable detector had to be chosen and purchased, since count-rate estimates indicated that the phototubes used on the Lamb-shift source test bench would be inadequate for the much smaller zero-degree beamline flux. The ABPIS needed some minor modifications to produce 550 or 1100 eV metastable atoms. The spin filter and all its utilities had to be mounted and installed in a very limited space between two other beamlines. A chamber for the detector also had to be procured. The decision to build the zero-degree line was made in mid-December 1991. By March of 1992 we were making our first measurements.

3.1.1 Metastable detector selection

The correct choice of an ultraviolet detector was critical for successful zero-degree line tests. We needed to measure the background signal, if any, and determine its source

and discover any other problems associated with beam from the ABPIS. However, we would not learn anything if the detector were not sensitive enough to Lyman-α radiation or if it were too sensitive to background signals.

The count-rate estimate was made based on the following factors. An incident beam current at the cesium oven of 50 μA was estimated to produce metastable atomic beam of 1×10^{14} metastable atoms/s. A significant fraction of the beam could be lost as it drifted the 4 m to the detector, because of the beam divergence. The beam "blow-up" was estimated by taking a ratio of the velocity components, transverse/axial, of the ion beam entering the cesium oven. The transverse component of the energy had been estimated at 5 eV; the axial component was the extraction energy of 1100 eV. This gave an angular divergence of the atomic beam of 1/15, implying a flux reduction of 1/730 for a 1 cm diameter beam at a distance of 4 meters downstream. If all of the metastable atoms in that beam were quenched creating ultraviolet light we could expect a rate of 1.4×10^{11} photon/s. The predicted output signal for the phototube which was previously used on the Lamb-shift test bench was femto-amperes. We had purchased an Ithaco 564 pre-amplifier, (see section 4.2), but even using the highest gain of 10^8 V/A, the signal would be much too small. We needed an increase in both gain and solid angle.

Several other types of detectors are used for the vacuum ultraviolet region of the spectrum. The possibilities inspected were photomultiplier tubes (Leo87), channel-multiplier plates (Wiz79), and photodiode (Ham91,Yna87) detectors.

The photomultiplier tubes (PMT), which operate as described by Leo (Leo87), were immediately attractive. The Hamamatsu model R2050 had a photocathode diameter of 5 cm and its gain could be as high as 10^6. Its anode sensitivity was 0.02 A/W for 121.6 nm photons. With a 1200 V bias on the photomultiplier tube, the expected signal would be 4.5×10^{-16} A / photon/s, so we could expect a signal on the order of

microamperes. This detector had the same spectral sensitivity as the R1187 phototube (see figure 2.6); its photocathode was CsI and the window was MgF_2. The photomultiplier tube was made to order by Hamamatsu at a unit cost of $2500.

Silicon photodiode detectors can be made of high-resistivity silicon wafers. The technical specifications are described in Ham87 and Yna87. They also have a radiant sensitivity of 0.02 A/W for Lyman-α photons. They are available from Hamamatsu in sizes as large as 5 cm^2 and they are quite inexpensive, around $300 each. However, they are sensitive to light from the ultraviolet to the infra-red, a major drawback because we knew that the ionizer produced copious amounts of light in the visible spectrum. Their spectral sensitivity was too broad for this application, although with the right filter they might have been acceptable. I did not explore this option in depth.

Channel-plate detectors, whose technical characteristics are described in Wiz79, are commonly used by astronomers for Lyman-α detection. Also called microchannel plate detectors, each one is an array of miniature electron multipliers oriented parallel to one another. They were first developed as amplification elements for image intensification devices. They are sensitive to both charged particles and energetic photons. Unfortunately, they are roughly 10 times as sensitive to 500 eV H^+ ions as they are to Lyman-a radiation so the ions would be a source of significant background. The channel-multiplier plates are expensive too, $3000 plus accessories, so they were excluded.

We purchased two of the Hamamatsu R2050 photomultiplier tubes and the matching E4229 bases. While we waited for the detectors, the rest of the preparations began.

3.1.2 Metastable Beam Transport

The beamline was built as short as possible axially to reduce the flux losses from the beam's divergence. A short bellows was used to attach a gate valve to the inflection magnet so that the zero-degree line could be isolated. After the gate valve, the spin filter was attached with Dependex mating flanges designed to mate to the spin filter ends. After the spin filter came the refurbished chamber for the photomultiplier tube (PMT) and the quench plates. Beyond the chamber we installed a beam scanner. All utilites for the spin filter and vacuum system were connected.

The vacuum chamber for the PMT and quench plate system was formerly used by Spencer (Spe91). The chamber had an inner diameter of 26 cm, a height of 15 cm, and Dependex flanges at its entrance and exit. After some modifications, the chamber had a port for the small turbo-pump, an isolated quench plate installed at -90° and the R2050 PMT at +90°. The quenching electric field was developed between the quench plate, which could be biased to 1 kV by a Kepco programmable supply, and a fine nickel mesh (95% transparent) stretched taut across the face of the PMT. The distance between the plate and the PMT face was 7.5 cm, so the electric fields could be as high as 130 V/cm.

Metastable atomic beams decay when the beam particles scatter from other particles, so metastable beam transport through the 4-meter distance required low pressure (long mean free path) in the beamline. For hydrogen atoms, the mean free path in air is of order 0.1 mm at 1 torr or 10 m at 10^{-5} torr. The spin filter and the detector chamber were evacuated using a 50 l/s Balzers turbo-pump backed by a mechanical pump with a molecular sieve in the foreline. Ultimately the pressure measured in the chamber was 3 x 10^{-6} torr.

The pressure was measured by cold-cathode gauges at two places on the zero-degree line, at the exit of the inflection magnet and at the detector chamber. Initially, when the gate valve between the inflection magnet and the zero-degree line was closed, the pressure at the detector chamber went from 5 x 10^{-6} to 5 x 10^{-5} torr. The helium leak chaser was used to look for leaks but none were found. The residual gas analyzer was used to measure the mass spectrum of the gas in the chamber, the major component was water. The spin filter is made of iron which absorbs water vapor from the air. Baking out the system for over 24 hours brought the pressure down to the 10^{-6} torr range. The spin filter will always need to be baked out when it has been exposed to air for longer than several hours.

Another type of quenching, "motional quenching", could occur when the metastable atoms passed through a transverse magnetic field. Motional electric fields can be calculated from $\boldsymbol{E} = \boldsymbol{v} \times \boldsymbol{B}$. For a 550-eV hydrogen atom moving in a 10 G magnetic field, the motional electric field is about 3 V/cm. There were two magnetic elements in the beamline between the ABPIS and the SFP that definitely could cause motional quenching, the Wien filter and the inflection magnet. The magnetic fields in the beamline are very important, not only because of motional quenching, but because of their effect on the quantization axis for the nuclear and electronic spin of the atoms in the beam. This important matter is discussed in section 3.4 .

3.2 ABPIS Metastable beam production

The ABPIS was not normally configured to produce beams at 0.5 to 1 keV with the cesium oven (lens 4) at ground potential. To understand the beam kinematics, it is easiest to look at a diagram like figure 3.2 which shows the potentials applied to the various

lenses and the ionizer. The values shown in figure 3.2 are representative values for negative deuterium beam production at a frame voltage of 80 kV. Usually lens 4 (the cesium oven) was not at ground potential for negative beam production and the electric fields present during normal operation after lens 4 would immediately quench any metastable beam created in the cesium oven.

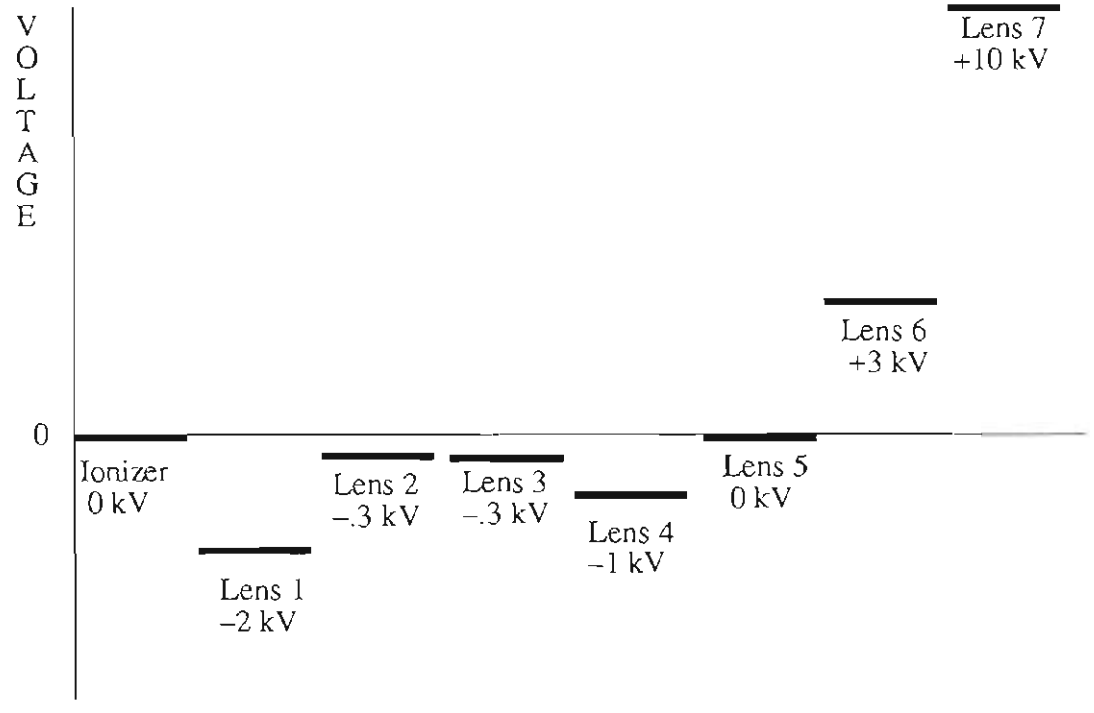

Figure 3.2 The lens potentials for negative beam production - ABPIS beam extraction system.

To change the biases so that we could produce positive hydrogen (deuterium) ion beams at 550 (1100) eV, the ionizer had to be biased to 550 (1100) V and Lens 4 (Cs oven) had to be at ground potential. This was possible because the ionizer internal parts, its sextupole magnet and its supports, are electrically isolated from the source frame and the ionizer chamber. There is an electrical connection external to the ionizer

vacuum chamber; to bias the ionizer one merely connects the power supply output to that feedthrough.

For the beam optics to stay the same, with the ionizer at 1100 kV and lens 4 at ground, lenses 2,3 and 5 had to be biased at positive instead of negative polarities. This can be understood by raising all the biases in figure 3.2 by 0.5 (1.1 kV) for hydrogen (deuterium) beams. Tests were made to determine if the same negative beam currents could be obtained with the ionizer and lenses biased in this different way, and equal beam currents could be extracted. This result was important; to produce metastable atomic beam the user would only need to ground lenses 4, 5, 6, and 7. The ionizer, and lenses 1, 2, and 3 could remain unchanged.

The next tests on the ABPIS were made to discover the optimum cesium oven temperature for metastable production. Also, information about negative and positive beam currents as a function of cesium temperature had not been formally recorded so these data were taken for completeness, as shown in figure 3.4. The broad peak versus temperature in the positive current reflects the fact that the data were collected faster than the cesium oven could reach thermal equilibrium; the oven controller did not always display the actual cesium reservoir temperature. Maximum positive beam is produced at roughly 90 C; adding cesium vapor provides electrons from ionization to reduce the space-charge electric fields so the beam optics improve, resulting in higher positive beam currents.

The metastable beam data in figure 3.4 were taken using a metastable beam detector that was installed in the ABPIS. This detector was one of the Hamamatsu R1187

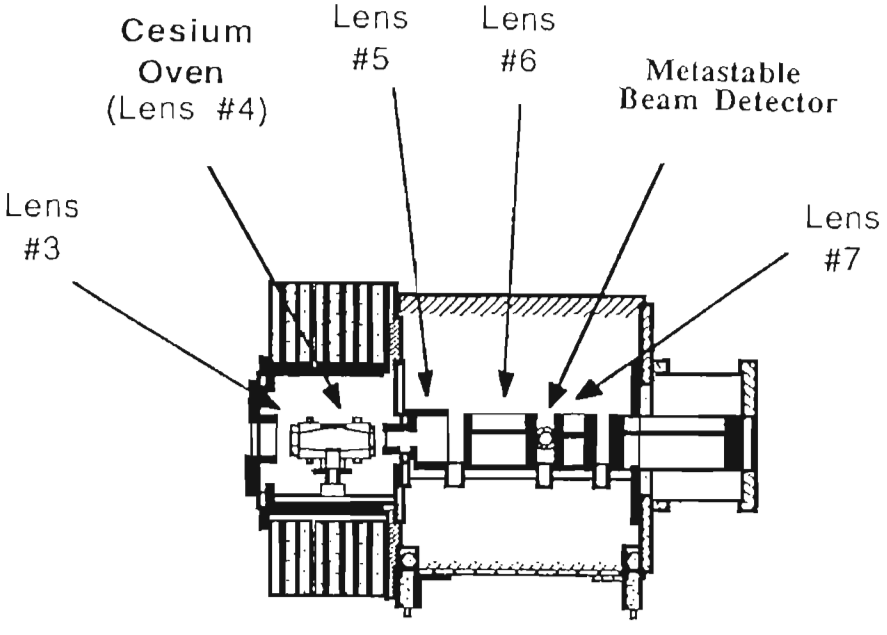

Figure 3.3 The ABPIS cesium oven and focussing lenses with the metastable detector.

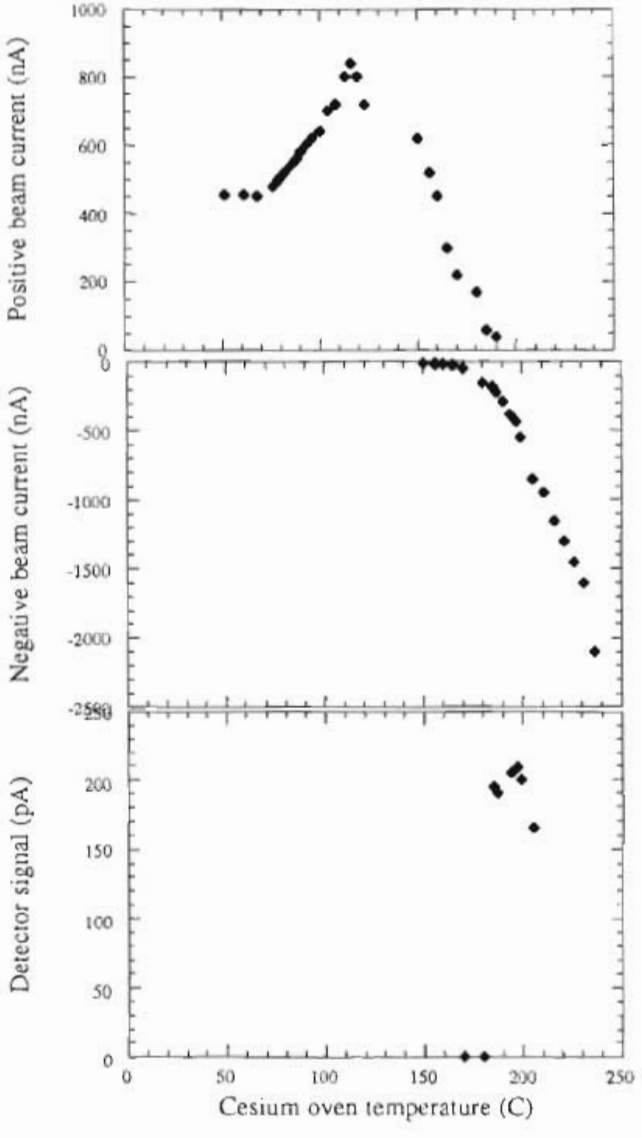

Figure 3.4 Positive beam current, negative beam current, and metastable detector signal as a function of cesium oven temperature. Note the vertical scale. Beam currents were measured on a Faraday cup located less than 1 meter downstream of the inflection magnet.

phototubes which was installed between lenses 6 and 7 in the cesium oven vacuum chamber, as seen in figure 3.3. The quenching field was supplied by biasing lens 7, while lenses 4, 5, and 6 were grounded. As a diagnostic, this detector was an invaluable addition to the ABPIS.

The ABPIS metastable beam detector provided signals of hundreds of picoamperes when unpolarized ion beam was produced by admitting H_2 or D_2 directly into the ECR ionizer chamber. In contrast, atomic beam from the dissociator produced signals of tens of picoamperes. The peak in the metastable signal occurred for lens 7 voltages of 500 to 700 V. Turning up the voltage on lens 5 quenched the metastable atoms upstream of the detector, providing a measure of the background signal. The signal-to-noise ratio for the ABPIS metastable detector was typically 25:1.

Having performed enough diagnostics to reliably produce metastable beam, we scheduled the first test on the zero-degree beamline.

3.3 Zero-degree Installation Results and Conclusions

The first results from the zero-degree beamline installation were both encouraging and discouraging. The good news was that there was plenty of signal in the photomultiplier tube (PMT) and that the hyperfine state separation was clearly observed. The bad news was that the beam that reached the detector chamber showed no evidence of polarization; the peaks were always of equal areas.

Using previous settings for the ionizer and lenses found while testing the ABPIS metastable detector, we were able to produce metastable beam and detect the Lyman-α decay radiation with the PMT almost immediately. With the spin filter magnets, rf power, and DC voltage turned off, the signal was 33 nA with the quench plate voltage on

and 10 nA with the quench-plate voltage off. With the atomic beam system valved off, the background signal was 2 nA, and with the ionizer valved off the signal was 1 nA.

The spin-filter electromagnetic fields were turned on, and after some tuning of the rf and DC fields, three 3 nA peaks from the unpolarized beam were observed above a 20 nA background. The signal-to-noise ratio for the peak signal was consistently 0.15/1.0 in spite of our best efforts to improve it.

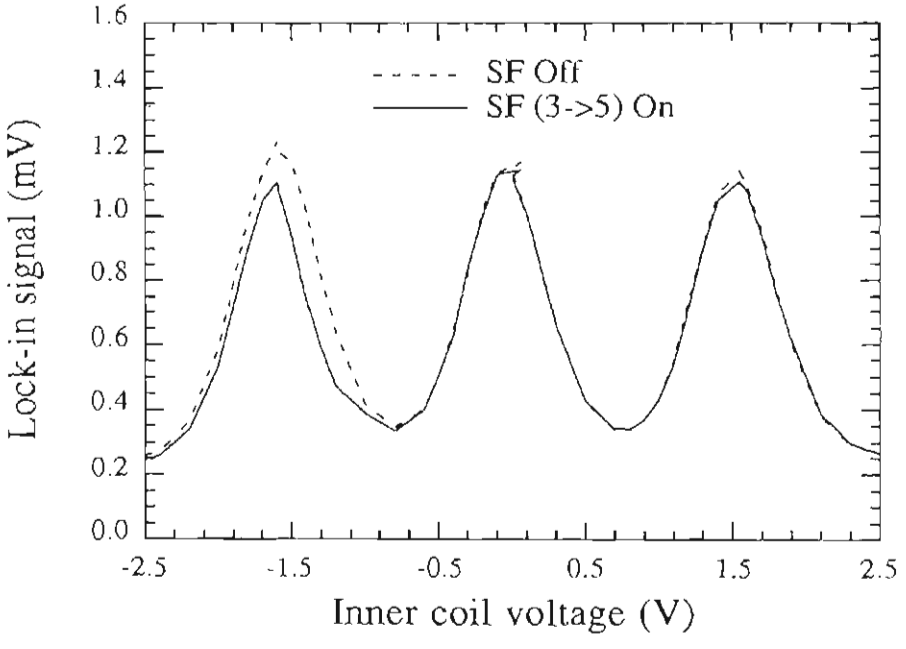

Figure 3.5 The null result on the SFP zero-degree beamline. This scan was taken by varying the axial magnetic field with the SFP inner coil. The lock-in amplifier accepted input at 2.8 Hz in synchronization with the quench plate voltage frequency.

Also, we saw only a very small effect, less than 10% (figure 3.5), associated with turning the rf power off and on in the ABPIS transition units. We checked the polarization using the lock-in technique and measured what appeared to be a polarized beam.

We sought to enhance the poor signal-to-noise ratio with a lock-in amplifier (CroPC) by looking at the difference in the signal from the PMT associated with switching the quench-plate bias turned off and on.

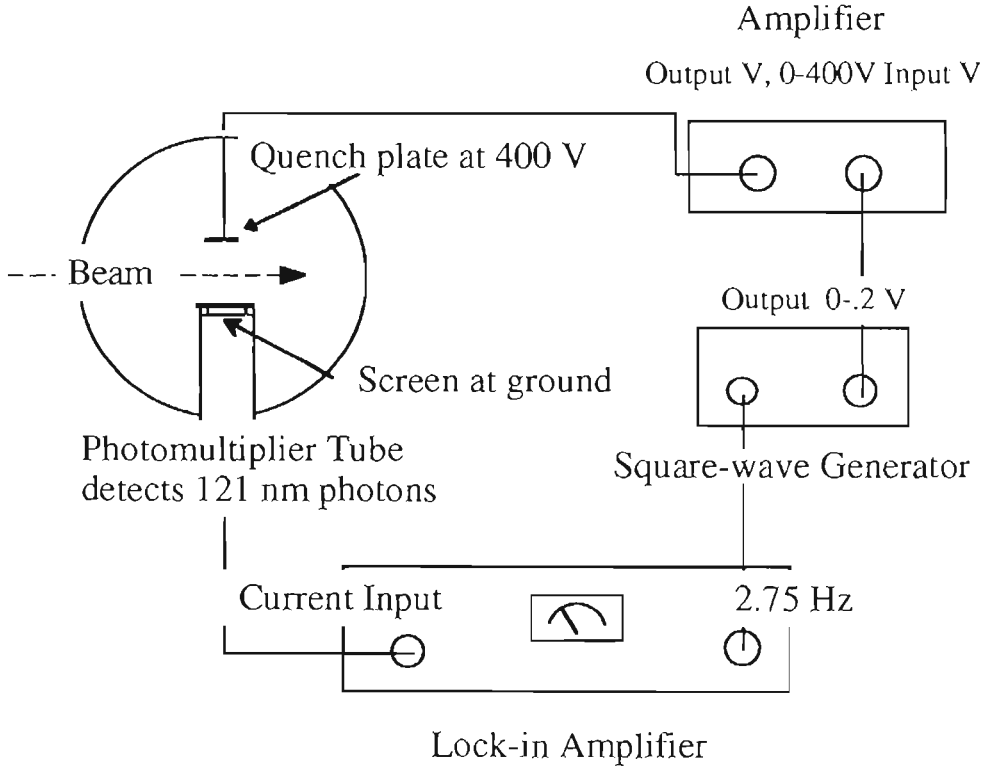

Figure 3.6 The lock-in amplifier noise suppression circuit

With the Kepco Model 10/20 Bipolar amplifier supply for the quench-plate programmed by the same square wave as was sent to the lock-in amplifier, the lock-in would suppress the noise at other frequencies, including white noise. The lock-in had another feature called "offset" which would allow us to "zero-away" the 20 nA background noise at the lock-in switching frequency. The schematic for this setup is shown in figure 3.6 . This worked quite well.

The final results of the zero-degree measurements proved that beam intensity was not a problem, but the SFP could not be used on the zero-degree beam leg because of depolarization by the magnetic field gradients. The beam polarization was destroyed by a combination of non-adiabatic spin reversals caused by axial field gradients and coupling of the nuclear and electronic spins in low magnetic fields. Although we saw three peaks of equal height and width, as expected for an unpolarized deuterium beam; there were only slight changes in the peak heights when the rf transition units were turned on, as shown in figure 3.5 above.

So, although the noise problem was avoided with the lock-in technique, we still did not observe polarization. We realized that magnetic field effects on the spins were probably the problem and so magnetic field measurements were made with a Hall probe. There were very low magnetic fields in the region between the Wien filter and the inflection magnet (less than 5 G) and the axial magnetic field actually changed sign at several spots along the beamline. These effects will now be discussed.

3.4 Spin Precession in Magnetic Fields

The emerging ABPIS polarized beam has a polarization introduced by passing through the atomic beam system rf transition units and sextupoles. That polarization

might not be maintained in the metastable beam as it moves along the source axis beyond the cesium region since there are magnetic field gradients present. What effect did the gradients have on the nuclear polarization carried by the metastable beam?

As discussed by Motz (Mot36), the Hamiltonian for the general case of an atom with nuclear spin **I** and electronic angular momentum **J** in a magnetic field B is $H = H_o + \mu_B\left(g_I\mathbf{I} + g_J\mathbf{J}\right)\bullet\mathbf{B} + \alpha(\mathbf{I}\bullet\mathbf{J})$, with the nuclear and electronic magnetic moments given as $\mu_{I,J} = g_{I,J}\,\mu_B$. The strength of the electron-nucleus coupling is given by $\alpha = \Delta W / J(2I+1)$, $I \geq J$. The critical field is defined by $B_c = \Delta W / \mu_B\left(g_I - g_J\right)$. The parameter $\chi = B/B_C$ can be used to characterize the energy splitting. For $\chi < 0.1$, the nuclear spin is coupled through the electron to the external field (Bre31). This is the so-called weak field regime. For $\chi = 1$, the nuclear spin is coupled strongly to *both* the electron and the external field, the so-called intermediate field regime. For $\chi > 3$, the nuclear and electron spins are coupled strongly to the external field and decoupled from each other. The critical fields are 63.4 G for metastable $2S_{1/2}$ hydrogen and 14.6 G for metastable deuterium. The following discussion is meant to provide an intuitive picture of how an external magnetic field effects the metastable atom nuclear polarization.

Let us consider how the magnetic fields encountered by the metastable beam might have affected the polarization, keeping the above characterizations in mind. Since the electron magnetic moment is about 2000 times larger than that of a nucleon, field gradients which would not significantly effect nuclear-polarized ion beams might be problematic for the nuclear-polarized atoms created in the cesium vapor for the spin-filter polarimeter measurements. This section discusses the effects of magnetic fields on the ABPIS metastable beam polarization.

If the axial magnetic fields along a beam trajectory were changing, then since the electromagnetic fields obey Maxwell's equation $\nabla\cdot\mathbf{B} = 0$ in a cylindrically symmetric

field there will be transverse components of the magnetic field calculable from the expression

$$B_r = -\frac{r}{2}\frac{\partial B_z}{\partial z}. \tag{3.1}$$

These radial components can cause the m-state populations of the nuclei in the beam to change.

An easy way to begin thinking about this is to consider a beam particle initially in an eigenstate of S_z, passing through a transverse magnetic field, B_x. The term in the Hamiltonian and the Schrödinger equation, $\mu \cdot B$, in that case will be proportional to $S_x B_x = 1/2(S_+ + iS_-)B_x$. The raising and lowering operators, S_+ and S_- imply a non-zero probability that the m-value changes, that is, depolarization can occur. In short, axial gradients may depolarize the metastable beam as it moves along the beamline.

The time development operator $U(t) = \exp(iHt/\hbar)$ takes on a simple form for a particle with magnetic moment, μ, in a constant magnetic field, **B**. Applying the time development operator to an eigenket of the system and then calculating the expectation values for the spin projections, S_X, S_Y, or S_Z, leads to the expression for Larmor precession of the spin about the magnetic field direction (Sak85). Such calculations are appropriate for the Wien filter rotation of positive or negative *ions* since the strong internal magnetic field is constant and the ions usually enter and exit the Wien filter over time scales that are short compared to their Larmor precession periods. Therefore, for polarized ions off-axis magnetic fields at the ends of the Wien filter are relatively unimportant.

When the magnetic field **B** has time-dependence in both its magnitude and direction, and when (as for 500 eV 2S hydrogen atoms) the time spent in the changing field is

comparable to the precession period, $2\pi/\omega = 2\pi\hbar/g\mu B$, the situation is more complex. The time-development operator can still be constructed from the Hamiltonian

$$H(t) = \boldsymbol{u} \cdot \boldsymbol{B}(t) = \hbar\omega(t) \propto \boldsymbol{S} \cdot \boldsymbol{n}(t) \quad \text{with} \quad \boldsymbol{n} = \frac{\boldsymbol{B}}{|\boldsymbol{B}|} \ . \tag{3.2}$$

but when the Hamiltonian is time-dependent, the time development operator can only take a simple form if it commutes with itself at different times, t_1 and t_2, for example. That means $H(t_1)$ and $H(t_2)$ must commute. But since $\left[S_i, S_j\right] = 2i\varepsilon_{ijk}S_k$, when the magnetic field direction, $\boldsymbol{n}$, is changing as a function of time, they do not commute. To calculate the time development of the system, the best starting point is the Schrödinger equation rather than the time development operator. The effects of the magnetic fields between the cesium oven and the SFP on the metastable beam polarization have been estimated (Tho93, Lem93) and they will be discussed in section 4.6 with respect to the data taken with the SFP installed on the ABPIS frame.

What magnetic fields were present on the axis of the ABPIS and the zero-degree beamline? Figure 3.7 show the measurements made with a Hall probe inserted into a jig on the ABPIS beam axis. The point z=0 cm is at the exit of the cesium oven and the point z=300 cm is located roughly 10 cm inside the inflection magnet, almost as far as the exit port at zero degrees. The magnetic field measurements shown in both plots were measured with the third coil of the ionizer system, C3, energized to 150 A, producing an axial field at the cesium oven in excess of 2000 G. The dashed curve on fig. 3.7a is the magnetic field magnitude calculated from measurements of all three components of the field with the Wien filter and the inflection magnet power on but set to zero. The second curve (z = 50-100 cm) on fig. 3.7b is the axial magnetic field measured on-axis with the Wien filter magnet and the inflection magnet power off. No transverse fields with

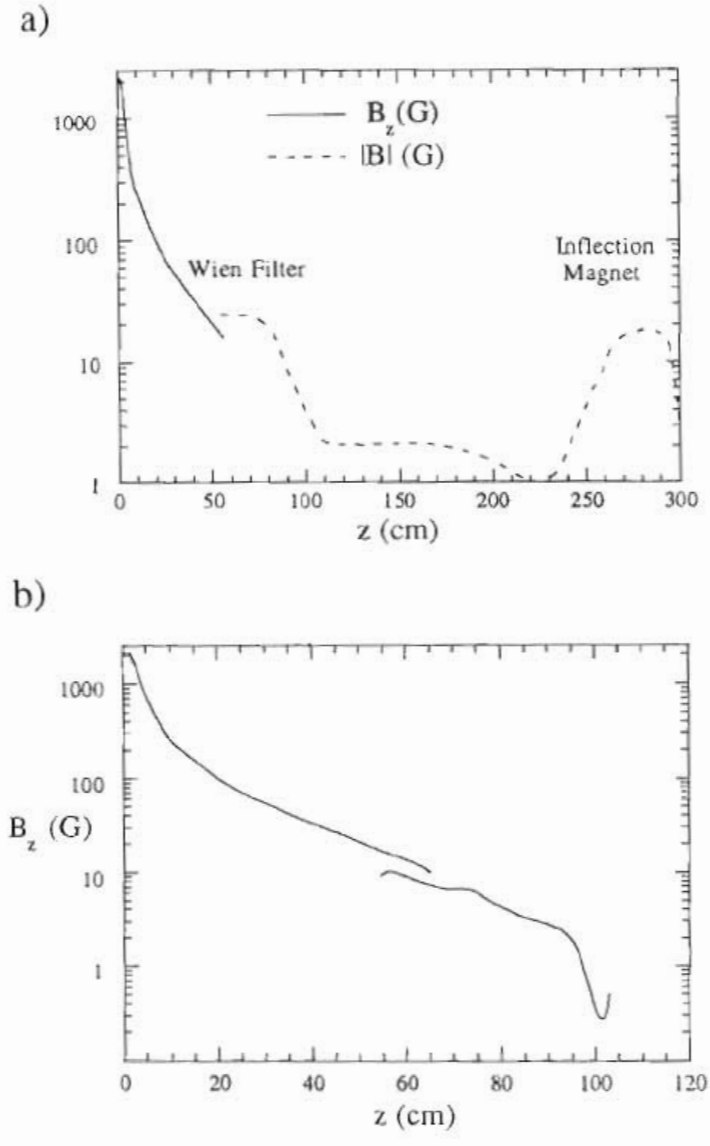

Figure 3.7 a) Magnetic field measurements between the end of the cesium oven, z=0, and the location of the SFP on the zero-degree beamline. b) Expanded plot showing the large field gradient immediately after the cesium oven.

magnitudes greater than 10 G were observed when the power supplies for those two magnets were off. For either case, the field in the region z=110 cm to z=210 cm drops to *below* the critical field value. To understand qualitatively what that means for the effect of the magnetic field on the spin, we consider a quantity called the precession length.

The precession length, $\ell = 2\pi V/\omega$, is the distance traveled, at speed V, for the spin to precess one radian about the magnetic field vector direction $\boldsymbol{n}$. In a 1 Gauss field, the precession length for a ground state H-atom (D-atom) at 550 eV (1100 eV) is ℓ = 17 mm. That means that every 11 cm the atom travels, it will precess one complete revolution aboutthe magnetic field direction. The precession length in the same 1 G field for a $2S_{1/2}$ metastable H-atom (D-atom) at 550 eV (1100 eV) is longer by a factor of 8, ℓ = 136 mm, because the magnetic moment of the metastable atom, and therefore the frequency, is lower by that factor. The precession length decreases inversely as B increases, so that for B=1000 G the metastable atom precession length is roughly 0.14 mm.

For a proton (deuteron), the precession lengths are about 2000 times longer than for the metastable hydrogen (deuterium) atom, since the nuclear magnetic moment is roughly 2000 times smaller than the atomic magnetic moment. As long as the external fields are far above the critical fields, the spins are decoupled.

Knowing that the critical field is 14 G for $2S_{1/2}$ deuterium, and that the precession length is on the order of 10 to 1 cm for a deuterium atom at fields from 1-10 G, the region in figure 3.7a from 30 cm < z < 70 cm takes on a new significance. A measurement made of the nuclear polarization after the metastable beam had passed through these intermediate field regions would show effects of coupling the nuclear and electronic spins in the region between the Wien filter and the inflection magnet.

Empirically we found that the effect was to destroy the metastable beam nuclear polarization, as seen in figure 3.5.

The spin filter polarimeter system itself had operated quite successfully. Since we understood why the polarization was lost, we knew that the SFP had to be mounted closer to the cesium oven and it was decided that a test on the ABPIS frame should be conducted. The description of that test and its results are the subject of Chapter 4.

Chapter 4

ABPIS Installation Test Results

The installation of the spin-filter polarimeter on the ABPIS was a resounding success. The spin filter separated the hyperfine states cleanly and the signal was clearly visible. (See figure 4.1 which is discussed in section 4.3.) The population changes for the magnetic substates were as predicted for all of the ABPIS rf transitions and the polarizations measured were consistent with previous measurements made with nuclear scattering polarimeters after acceleration through the TUNL tandem accelerator. This chapter discusses the experimental apparatus including the spin filter parameters (section 4.2), and the data-taking electronics (section 4.3), the results from the ABPIS installation of the SFP (section 4.4), the measurements made using the SFP (section 4.5), and concludes with suggestions for future work (section 4.6).

These data were collected during four days of a two-week test in May 1992. The first polarization scans were obtained on the second evening of the experimental time after the removal of the Wien filter so that the SFP could be installed in its place. We studied the SFP-ABPIS system for two days and then spent two days testing the new medium-field transition units (Din93). The remainder of the experimental time was spent on maintenance and re-installation of the Wien filter.

It is noteworthy that previous experimental tests of the medium-field units performed in February 1992 had been painstakingly slow. The debugging and fine-tuning of the

MF units was greatly facilitated by the SFP hyperfine state information - much more complete information at the ABPIS than can be obtained with any nuclear-scattering polarimeter.

4.1 Motivation for Temporary Installation on the ABPIS

Since the spin orientation could not be maintained on the zero-degree leg without the addition of guide coils which would inhibit normal operation of the source, we decided to mount the spin-filter polarimeter on the ABPIS for one proof-of-principle test run. The SFP was mounted in the position usually occupied by the Wien filter (see figure 4.2). Our main objective for this test was to determine whether or not the spin filter could operate as a polarimeter if it were permanently mounted on the source frame. If the polarimeter worked there, then complete tests of the strong- and weak-field transitions units could be made. Also, we felt it was important to characterize the polarimeter operation under normal source operating conditions, that is, conditions when the ABPIS was optimized for production of polarized ion beam for experiments.

Development of "medium-field", MF, transition units (Din92) for the ABPIS was proceeding in parallel with the polarimeter project. It was decided that the testing of both the new polarimeter and the transition unit could occur sequentially during the same run since the spin-filter polarimeter could be used to measure quickly and directly the polarizations obtained with the MF unit.

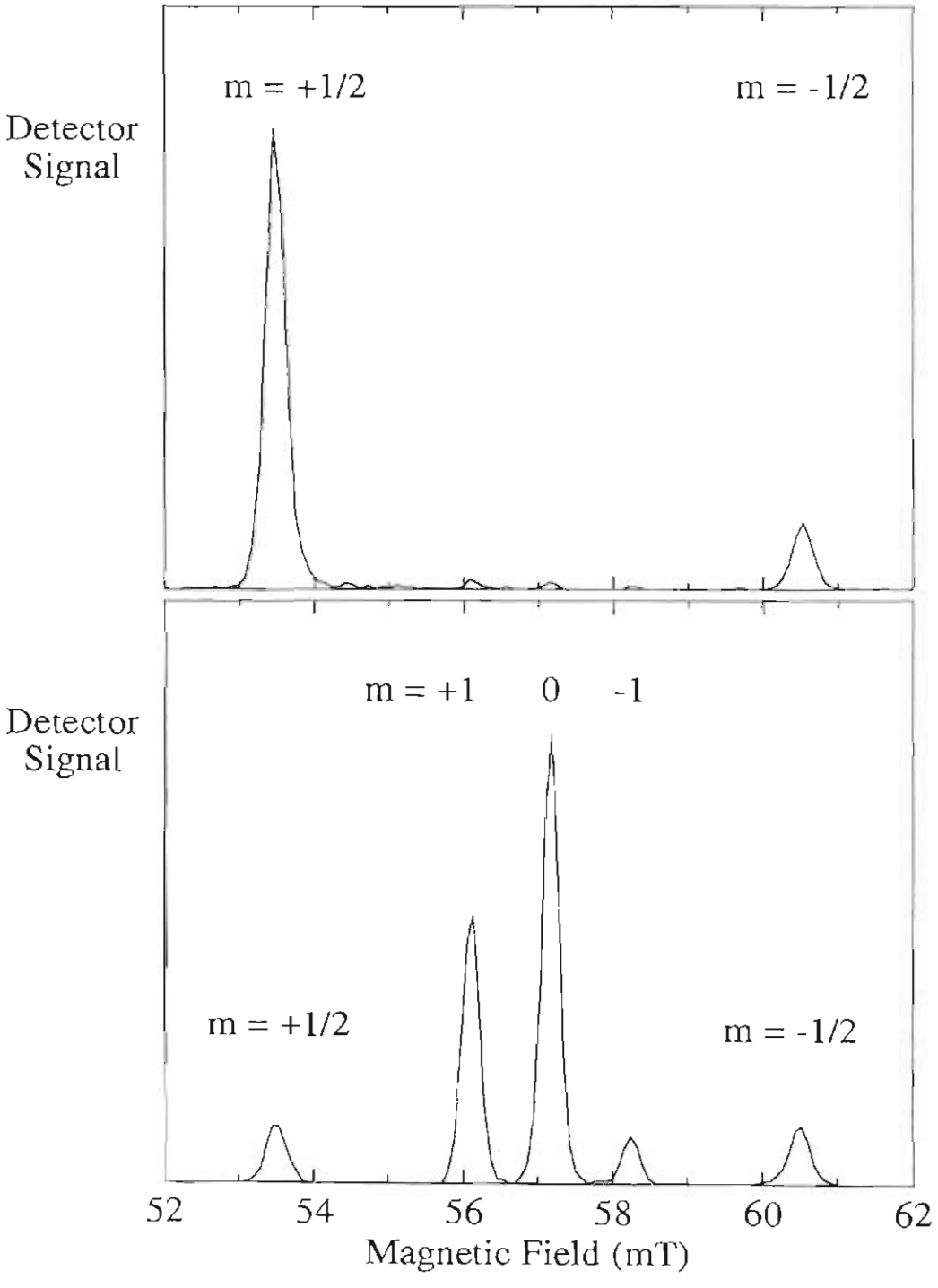

Figure 4.1 Top plot is a proton scan, P_z=0.73. Lower plot is a deuteron scan P_z=0.29,P_{zz}=-0.71.

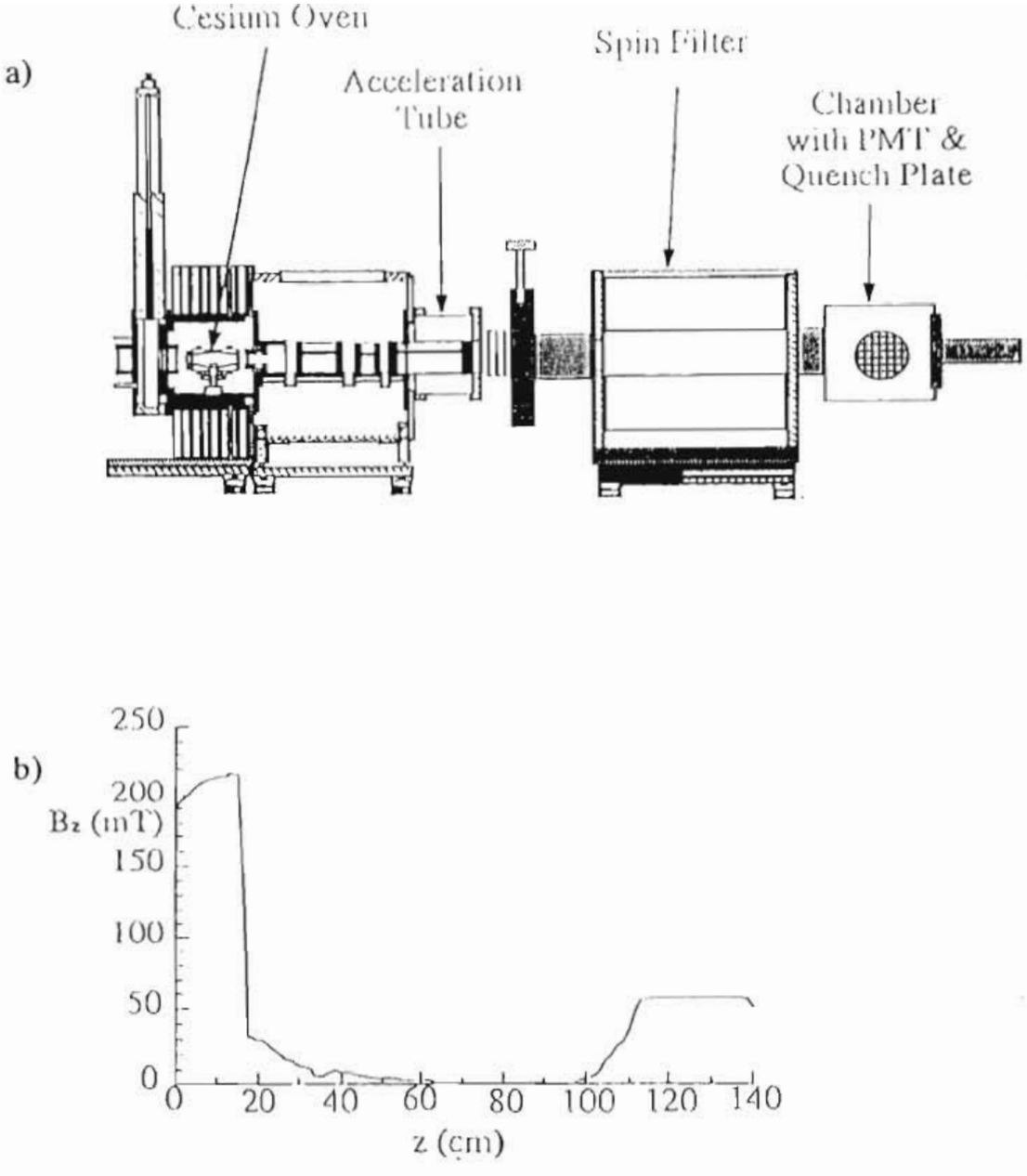

Figure 4.2 a) The SFP installed on the ABPIS frame. b) The axial magnetic field along the beam axis of the SFP-ABPIS system.

4.2 ABPIS Installation - Spin Filter Polarimeter Operation

We removed the Wien filter from the source frame to make room for the spin filter and the detector chamber. The spin filter was mounted in its saddle on the aluminum plate where the Wien filter is usually mounted and aligned. Its alignment was performed using an optical axis determined by sighting through a telescope placed at the zero-degree marker in the low-energy bay to an optical target placed in the 2" Dependex fitting at the end of the first ABPIS acceleration tube. Optical targets were placed at both ends of the spin filter and at the end of the detector chamber; then the spin filter and chamber positions were adjusted until all the cross-hairs were centered.

All of the power supplies for the SFP were mounted in an electronics rack which was placed on a wooden dolly for mobility, and the dolly was rolled inside the source cage. The polarimeter power supply connections and interlocks for oil-cooling are outlined in Appendix 1 along with a list of the necessary checks before pump-out for installing the SFP.

4.3 Polarization Measurement Scheme

The polarization spectra were obtained by ramping the inner coil field up and down so that the magnetic field inside the spin filter varied from roughly 520 to 620 G in 128 steps during one ramp period of about 1 min/scan. The ramp stepped the magnetic field by controlling the programming voltage for the inner coil power supply, the steps were roughly 1 G/ step. The ramp swept up and then down for each scan, and those data were

digitally summed. Each channel contains data from one increasing field scan added to data from one decreasing field scan.

The pre-amplified signals from the PMT was sent synchronously to an analog-to-digital (ADC) converter together with the ramp signal controlling the magnetic field amplitude. These signals were both DC, which was not acceptable to the ADC units, so a pulser signal at roughly 10 kHz was used to generate gates for the ADC's, effectively chopping the signals from the ramp and the PMT. The electronics schematic for the data-taking is shown in figure 4.3.

The peaks are clearly visible and well-separated, but there was an enormous background in many of the spectra, as shown in figure 4.4, which is an early run taken using the strong field (SF) transition unit to provide deuteron polarization, $P_z = 0.27$, $P_{zz} = 0.60$. The theoretical maxima for this transition are $P_z = 0.33$, $P_{zz} = 1.0$. Figure 4.4a displays the raw data from which background was subtracted to produce figure 4.1. Figure 4.4b shows a different background subtraction than that used for figure 4.1. The two different subtractions agreed for P_z to $\pm$ 0.02, but for P_{zz} the agreement was not so good namely $\pm$ 0.09.

At the beginning of the two-day run, the hyperfine states provided peak PMT output currents (measured on an electrometer) of 300 nA on a background of 160 nA. The background dropped significantly, to 60 nA, when the gate valve between the atomic beam system and the ECR ionizer was closed, so the background was beam-related.

With the quench-plate voltage off and the gate valve open, there was still 100 nA of signal on the PMT. This "unquenched" signal was probably caused by a field developed by beam striking the quench plate and charging it to some potential; this effect was present on the LSPIS test bench. In that set-up it was not always necessary for the quench plate bias to be turned on at all.

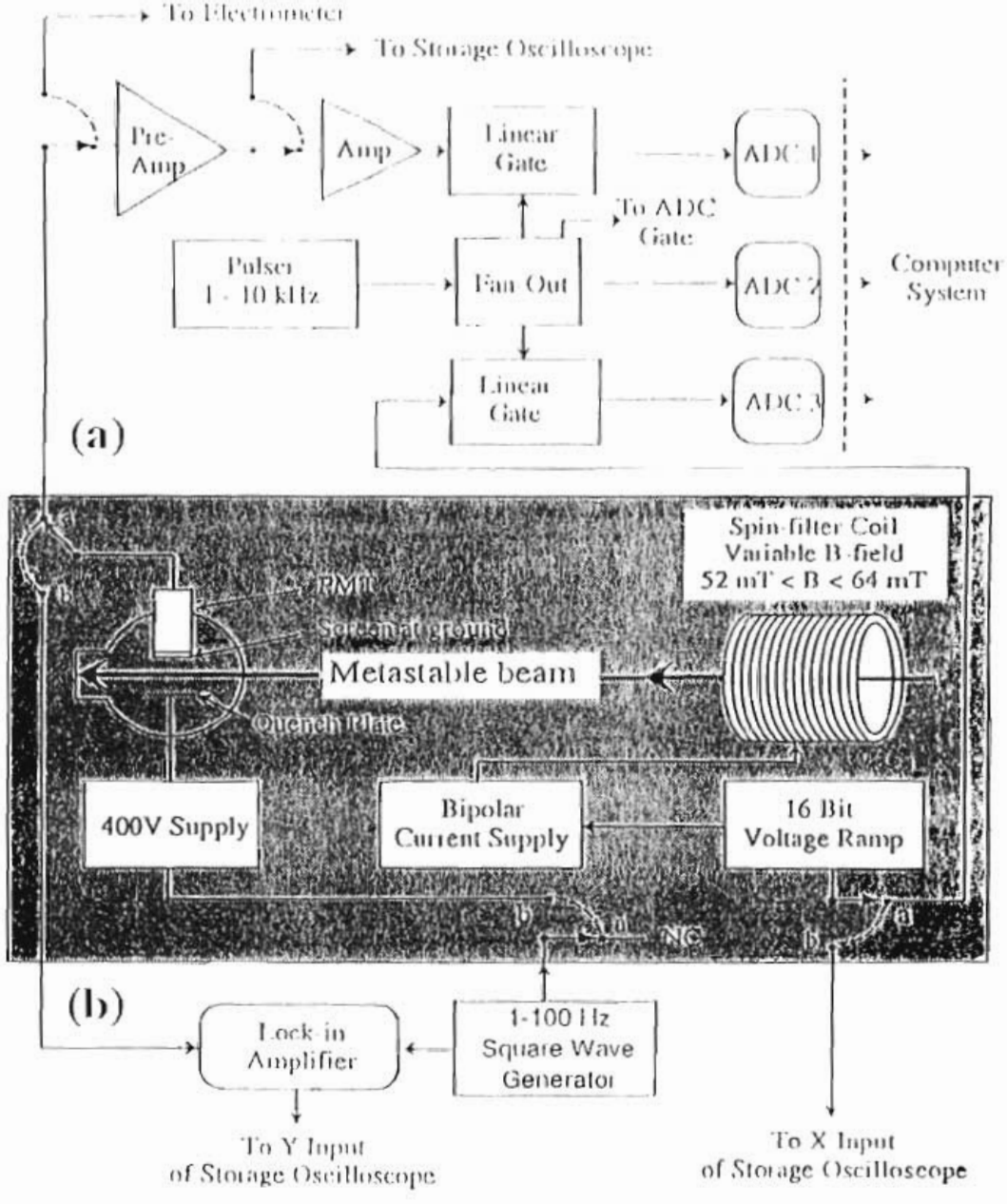

Figure 4.3 Block diagram for the electronics used to store SFP scans in the computer.

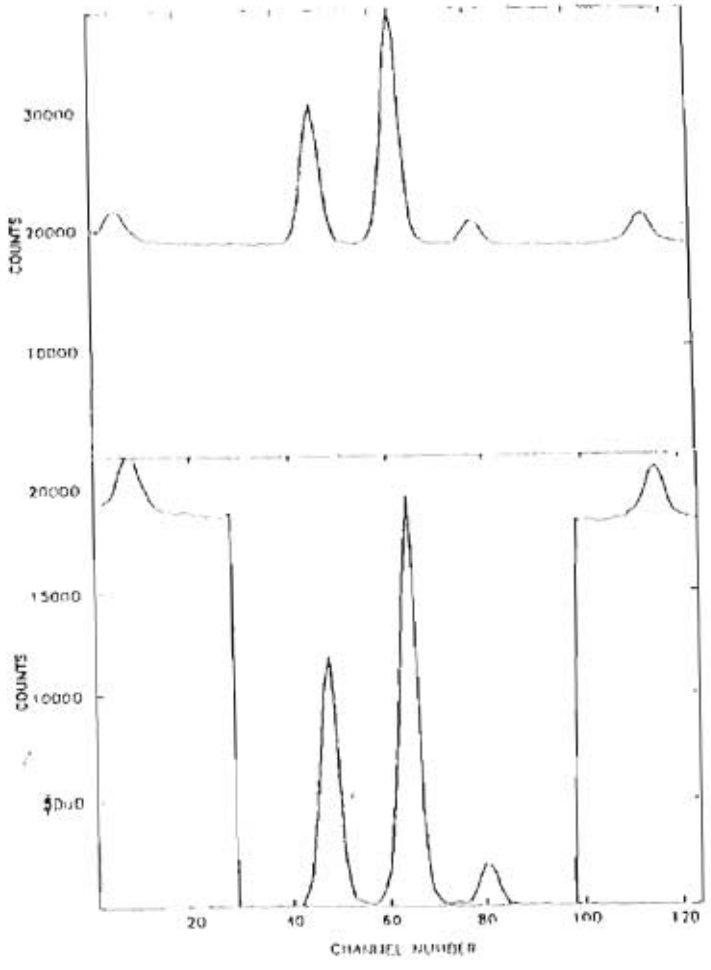

Figure 4.4 a) Raw data as stored in the computer. The x-axis is the channel number corresponding to the programming voltage sent to the inner coil, which was proportional to the inner coil current and the y-axis is the processed PMT signal from an increasing and a decreasing scan summed. The peaks are, from left to right, hydrogen with proton spin-up, deuterium with deuteron spin-up, deuteron spin-along, deuteron spin-down, and hydrogen with proton spin-down.
b) After a parabolic background subtraction using points at either side of the three deuterium peaks and in the valleys between the deuterium peaks, $P_z = 0.27$, $P_{zz} = -0.73$.

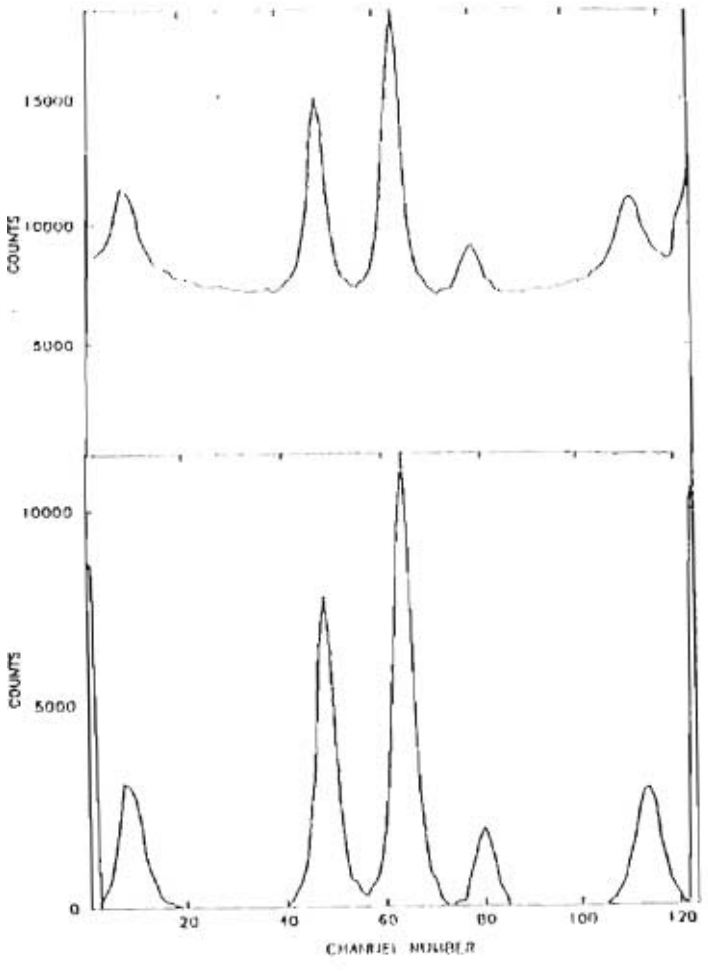

Figure 4.5 a) The same transition, SF2(3–>5), as in figure 4.4 taken earlier when the ECR ionizer had not been evacuated for very long and the rf power into the SFP rf cavity had not yet been increased.

Raising the rf power into the SFP tuned cavity flattens the background, as can be seen by comparing figures 4.4 and 4.5. The flatter background makes it much easier to extract the peak areas consistently. But, differences of 2.5% in the calculated beam polarizations were observed in successive runs when there had been no ABPIS or SFP parameter changes made. Sets of 20 runs with polarized beam and 10 runs with unpolarized (ionizer beam) beam were taken to establish the deviation from run to run.

For these data sets several different background subtractions were tried yielding a mean and standard deviation for the extracted polarization values. Polarization values quoted are the mean values. For these runs, the tensor polarization is the most sensitive to the background subtraction because the background was not always flat under the middle (m=0) peak. Higher rf power should correct that problem. The vector-polarization measurements were much more consistent and the results agreed within the individual standard deviation for all background subtractions. The following standard deviations were calculated including effects of differing background subtractions: for the 20 deuteron polarized runs - $P_z = 0.25 \pm 0.03$ and $P_{zz} = 0.80 \pm 0.05$ and for the 10 deuteron unpolarized runs using deuterium bled into the ionizer chamber - $P_z = 0.02 \pm 0.02$ and $P_{zz} = 0.00 \pm 0.02$.

The background is PMT bias-dependent. If the peak signal is well out of the noise then the gain (PMT bias) could be decreased and the background was lower. If the peak signal was not as strong, then as the gain was increased to make the signal large enough for the ADC, the background increased.

The PMT gain depends on the signal size and the data were not corrected for this effect. The peaks shape and areas might be different if a gain stabilization circuit were added. Since the peak areas are combined using equations 1.1, 1.2, and 1.3 for polarization measurements, gain stabilization may not significantly affect the values but

the effect should be measured in order to reduce the uncertainty in the measurement as much as possible. If the SFP measurements are to be as precise as the quench-ratio measurements then all sources of error must be considered.

4.4 Polarization scans on a digitizing oscilloscope

The data could also be stored on a Hewlett-Packard 54600A digitizing storage oscilloscope. The experimentalist could adjust the transition units or focusing elements on the source and observe the effects on the beam polarization in real time. The scope was run in X-Y mode with the inner coil programming voltage supplying the x-signal and the PMT pre-amp supplying the y-signal.

We observed an interesting effect as the inner coil sweep frequency was increased. As the magnetic field swept first up and then back down, the peaks appeared at different x-positions, as if the whole pattern had been offset. The offset was frequency dependent, that is, the faster the inner coil was swept, the larger the offset. Since the x-position of the sweep was determined by the programming voltage sent to the inner coil, rather than by the field or current of the coil itself, this effect can be explained by the self-inductance of the spin-filter coil system. With the resolution of 1G/ channel at sweep speeds of 1 min/scan the effect is not discernible, but at higher sweep frequencies the summed peaks for the two sweep directions broaden and begin to overlap.

This problem would be surmountable by using the digitizing scope's RS232 port. The data from the scope can be dumped to a personal computer and accessed through a communications program such as PRO-COM or KERMIT. Then the data could be easily sorted by sweep direction. The data from the scope would also not carry any errors from the gating of the signals required by the ADC units.

4.5 Measurements with the SFP

While the SFP was mounted on the ABPIS, we characterized, quantitatively, many source parameters. The polarization versus rf power was measured for the strong field (SF) transition units, polarization versus sextupole 2 current, and polarization versus cesium oven temperature. Measurements that had previously taken hours or days were accomplished in minutes. We also tested the SFP at lens settings more like those used for negative beam extraction.

4.5.1 The transition units: SF1, SF2, WF, & MF

One of the simplest ways to maximize the beam polarization with the SFP does not use either the digitizing scope or the ramp-ADC electronics. The PMT output can be connected directly into an electrometer. Then the inner coil field is set for an appropriate field to cause the hyperfine state resonance (on a peak) and the transition unit to be tuned is turned on. Tuning the transition unit can be accomplished by maximizing the PMT signal on the largest hyperfine state peak. This makes maximizing polarization at the source as easy as steering the beam.

For deuterium beams the following tests were performed: rf power scans for strong field (SF)1 (2–>6) and (3–>5), SF2 (2–>6) and (3–>5), SF2 (3–>6) and weak field (WF) 2 (1–>4). These results showed that the SF units need very little rf power to polarize the beam (see figure 4.6). For hydrogen beams the SF1(2–>3) and WF2 (1–>4) transition units were tested. Also the new medium-field (MF) transition units (Din93) were installed during the second phase of the run and tested. The MF units replaced the WF units which had inadequate magnetic shielding.

a)

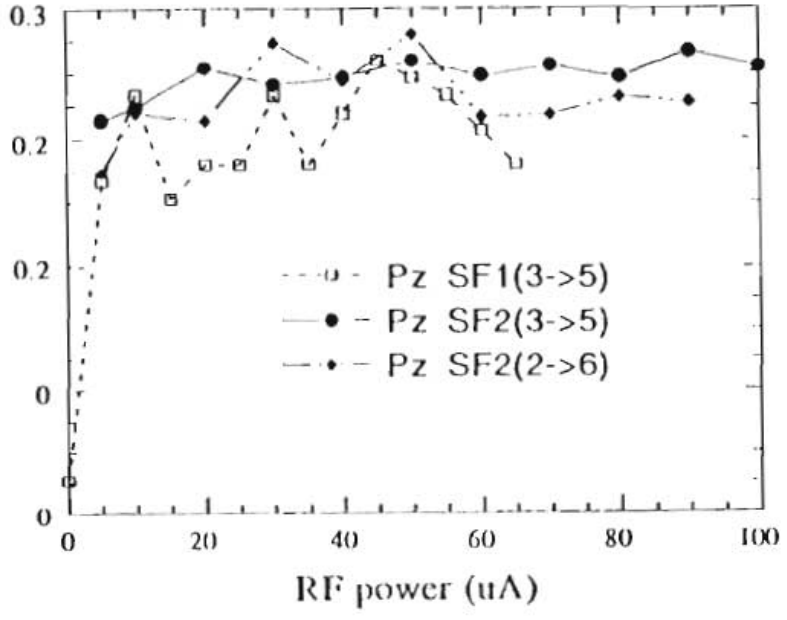

b)

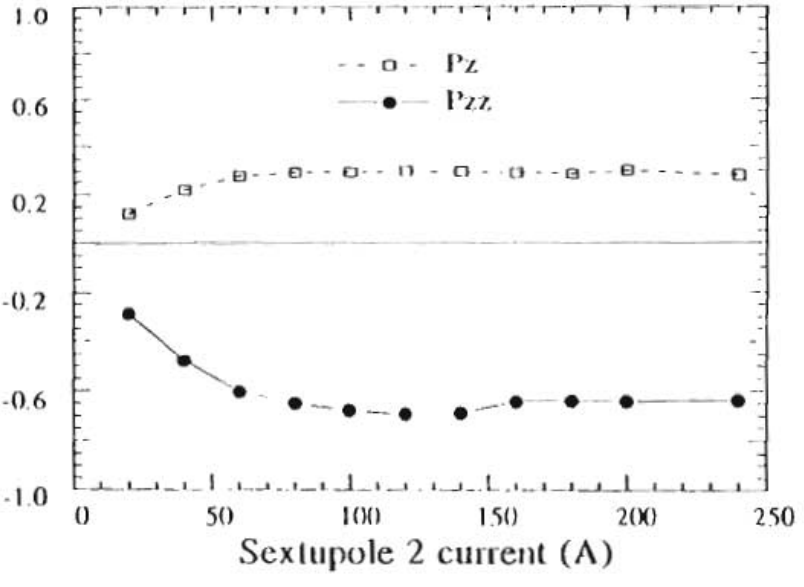

Figure 4.6 a) Deuteron vector polarization versus rf power for various transition units. b) Deuteron vector and tensor polarization versus sextupole 2 current.

The testing of the MF transition units, previously a several day-long tandem accelerator nuclear-scattering experiment, was accomplished in several hours.

4.5.2 Polarization vs cesium temperature & lens settings

Spin-filter polarimeter measurements would be easier to make if the cesium oven temperature and the lens biases could be set to the same operating levels as used for positive/negative beam extraction. For that reason, tests were performed to determine the range of operating parameters for the SFP.

We determined the range of cesium oven temperatures over which the SFP could operate (see figure 4.7). For lower cesium temperatures, as would be used for positive beam production, the vector and tensor polarization measurements were constant to 8% over a temperature range from 103 C to 170 C. Over a wider temperature range, from 100 C to 250 C, the polarizations extracted were constant to about 13% using the same background subtraction technique over the temperature range. At 104 C, $P_{ZZ} = 0.660$ and at 250 C $P_{ZZ} = 0.664$, there was no systematic rise or fall in the polarization.

The PMT signal intensity displayed in figure 4.7 was extracted by summing the background-subtracted areas from the three deuterium peaks. Since the PMT voltage was changed from -1400V to -1200V at a Cs oven temperature of 154C, the sums for the temperatures above 154C had to be divided by the associated gain change of about 3. No other corrections were made to the sums. The lower level discriminator on the ADC was also raised when the gain was changed. At 100 C the signal-to-noise was 1.7 and at 250 C S/N was 2. This result supports the very important conclusion that, for the 90 C (240 C) cesium oven operating temperature used for optimal positive (negative) polarized ion production, the PMT signal is still 70% (40%) of the maximum value.

In a subsequent experiment, the ionizer and lenses were also reset to parameters similar to the usual operating parameters. It was discovered that the SFP could still measure polarization with the following lens configuration: the ionizer at ground potential, lens 1 at 0.5 kV, lenses 2 and 3 at 0.23 kV, lens 4 at 0.30 kV and lenses 5, 6, and 7 off. So, since the lens supplies are programmable, with the polarimeter mounted on the ABPIS frame a polarization measurement could be made by inhibiting the data acquisition, remotely

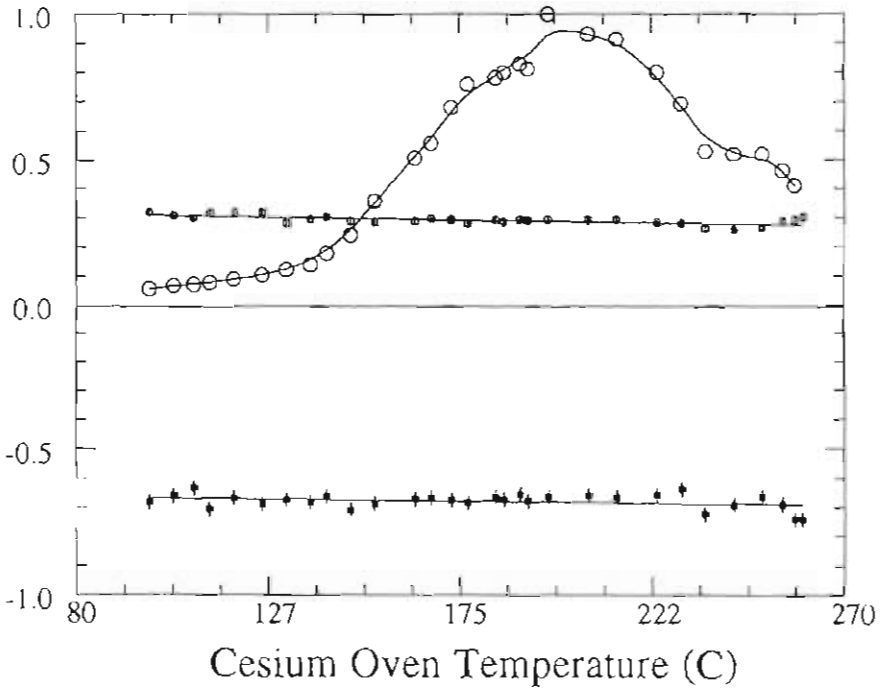

Figure 4.7 Deuteron vector (open squares) and tensor (closed squares) polarizations plotted with relative signal (open circles) from the metastable detector system versus cesium oven temperature. Maximal negative beam occurs at 250-270C and maximal positive beam at 95C.

resetting the lens biases using the Texas Instruments computer, and taking a two-minute measurement with the SFP. Data from the SFP could be stored concurrently for an "almost on-line" polarization measurement.

4.6 Conclusions and Future Outlook

The SFP should be mounted on the ABPIS for general use. It has been shown to be a valuable tool for measuring relative beam polarizations in a way which provides more information than any other available technique at TUNL. Once the SFP polarization measurements have been checked by comparison to other polarimetry standards, it will be useful as an absolute polarimeter. All that remains is the characterization of the effects of acceleration and focusing on the ABPIS beam polarization.

Some improvements to add: 1) a carefully considered collimation scheme might improve the signal/noise ratio enough that background subtraction effects would become negligible. 2) The digitizing oscilloscope data-taking capabilities should be used so errors are not introduced by needlessly complicated data-taking schemes. 3) Gain stabilization should be provided for the PMT. 4) The depolarization effects (Tho93) should be verified for this data and any taken in the future.

If a suitable design could be found to produce the constant magnetic field needed for spin-filter operation without using the heavy, oil-cooled iron coil system, installation would be much more attractive. One drawback to the present SFP system is that it has oil-leak potential, both internally to the vacuum system and externally.

It has been suggested that the axial field of the coil C3, used to maintain the beam polarization axis in the ABPIS cesium oven region, might be shaped with some highly permeable magnetic materials. This location would have the added advantage of

minimizing depolarization effects in gradient fields, but it will be hard to install a PMT there.

The 0.5 G uniformity required may be difficult to achieve with such a design, but for slower atoms that spend a longer time passing through the spin filter, a shorter region of uniformity might suffice. Although the cross-section for metastable formation peaks at 550 eV (1100eV) for hydrogen (deuterium), with an efficient detection system the incident beam energy could be lower.

It has also been suggested that the SFP could be used to analyze the polarized atoms of a polarized gas jet target. The idea (Pri93) is to extract a small fraction of the target atoms at 550 eV and pass them through a SFP. My experience with metastable beam detection and hyperfine state separation leads me to the conclusion that this could be done as long as the magnetic fields were carefully mapped. It is harder to retain the nuclear polarization in the metastable atoms than it is to detect them.

The asymmetry in the "unpolarized" hydrogen peaks (the outermost peaks in figure 4.1b) has been confirmed. Tests of the background subtraction show that there is a real asymmetry in the data. It is possible that the permanent sextupole magnet in the ECR ionizer is causing the asymmetry. From the Breit-Rabi diagram, figure 1.2, it can be seen that at low magnetic fields the slope of the energy levels is different for the electron spin-up proton spin-up states than the electron spin-up proton spin-down states. The slope of the energy versus magnetic field is the effective magnetic moment, so state 1 would be more strongly focused in the magnetic field than state 2. This should be a small effect, and it is. To test this theory the magnetic field in the ionizer should be varied and the resulting "unpolarized beam" polarization observed.

The SFP is an elegant generally useful device combining atomic and nuclear physics technologies which probably has more applications than have been imagined so far.

Chapter 5

A Study of the Alpha-Particle D State

As mentioned in the introduction, this thesis has two separate and distinct parts. The first four chapters, about the spin-filter polarimeter, describe an atomic physics technique for measuring the nuclear polarization of an ion beam. This chapter is pure nuclear physics. It describes the experimental work, the data analysis, and the distorted-wave Born approximation calculations which were performed as part of a collaborative study of the alpha-particle D state.

This chapter describes the measurement and analysis of the $^{50}Ti(\vec{d},\alpha)^{48}Sc$ reaction at E_d=16 MeV to study the α-particle wave function. Information from this reaction formed part of an extensive study, $^{48}Ti(\vec{d},\alpha)^{46}Sc$ at E_d=22 MeV, and $^{58}Ni(\vec{d},\alpha)^{56}Co$ at E_d=16 MeV and 22 MeV, using realistic microscopic wave functions to model the α particle (Cro93, Cro92).

5.1 Introduction

In 1896 Henri Becquerel observed that his well-wrapped photographic plates blackened when they were near certain mineral samples; those samples of ore contained radium. In 1898 the Curies separated the radium from ore to study the emissions that had blackened Becquerel's photographic plates. Three distinct types of emissions were

discovered and named: alpha-particles (^{4}He nuclei), beta-rays (electrons or positrons), and gamma-rays (electromagnetic radiation). Early nuclear physicists discovered that these first two emissions change the chemical properties of the elements; they were the first successful alchemists.

The α particles were first isolated from the beta and gamma rays by deflection in an electromagnetic field by Rutherford in 1903. Rutherford also proved that the α particle was actually the ^{4}He nucleus by measuring helium spectral lines in a thin-walled evacuated chamber irradiated by alpha-particles. Other nuclei, deuterons for example, or protons, are usually *not* spontaneously emitted by nuclei, but many heavy nuclei spontaneously emit α particles. What is different about α particles?

The α particle is very stable and tightly bound, E_b = 28 MeV; thus α-particle emission enables a nucleus to emit a light disintegration product with a large release of kinetic energy. This begs the next question, why is the α particle so tightly bound? Although the nuclear interaction in light nuclei is dominated by the long-range OPEP (one pion-exchange potential), the α-particle high binding energy indicates the presence of strong short range interactions as well. Its configuration of four nucleons coupled to a total angular momentum of zero provides a unique "laboratory" for studying these short-range components of the strong interaction.

The deuteron is the antithesis of the alpha-particle. It is very loosely bound and its two nucleons couple to a total angular momentum of one unit. It is a distorted particle, with a non-zero electric quadrupole moment and a magnetic dipole moment which differs from the sum of the proton and neutron magnetic moments. There is an ℓ=2 or D-state component of orbital angular momentum between the neutron and the proton. From the deuteron D state, nuclear physicists learned of the long-range nuclear tensor interaction. In the deuteron, with its two nucleons, it is relatively straightforward to calculate the

electric quadrupole moment or the magnetic moment from a nucleon-nucleon (NN) interaction and therefore to test different models of the NN interaction.

5.1.1 TAP relationship to D states of light nuclei

The D state of the deuteron and of the three-nucleon bound states, ^{3}H and ^{3}He, can also be determined indirectly by measuring the tensor analyzing powers (TAP) for single-nucleon transfer reactions: ($\vec{d}$,p), ($\vec{d}$,n), ($\vec{d}$,^{3}H), and ($\vec{d}$,^{3}He). Radiative capture data from the reactions ^{2}H(n,γ)^{3}H, and ^{2}H(p,γ)^{3}He have also been analyzed to extract information about D states of light nuclei.

In the α-particle, studying the tensor interaction via the D state is not that simple. As a matter of fact, one might expect such a tightly bound $J^\pi=0^+$ particle to be entirely spherical. There is no spectroscopic quadrupole moment, and no magnetic moment, no direct evidence for a D state in the α-particle. Reliable studies of nuclear structure place energy levels and assign spins to levels in heavy nuclei using α-particle decay systematics based on the S-state configuration of the α particle.

But, there is a D state in the α-particle, first postulated by Schwinger (Sch42). Nuclear physicists found experimental evidence for the α-particle D state using some of the same techniques that were used in investigations of the two- and three-nucleon system's D states, transfer reactions and radiative capture reactions. Plattner produced the first experimental evidence for an α-particle D state (Pla75). Santos *et al.* suggested that the TAP for ($\vec{d}$,α) transfer reactions are also sensitive to the α-particle's D state (San 84). Radiative capture, ^{2}H($\vec{d}$,γ)^{4}He, studies seemed to have a strong D-state dependence in the TAP also, but D-state information from the capture reaction is clouded by uncertainties in the reaction mechanism.

We chose to study the α-particle D state by using ($\vec{d}$,α) transfer reactions which are sensitive to the deuteron-deuteron configuration in the alpha particle. Although the two-nucleon transfer studies are model dependent, with a suitable choice of reaction the uncertainties in the model can be minimized.

5.1.2 Realistic wave functions

The most attractive feature of the analysis of the ($\vec{d}$,α) reactions used in this study is the realistic variational wave functions calculated by Schiavilla, Panharipande and Wiringa used to describe the α particle (Sch86). The method of Schiavilla, Pandharipande, and Wiringa is a general Monte-Carlo variational calculation of the momentum distribution of nucleons in A=3,4 nuclei. The calculations were done for all possible two-body configurations of these nuclei. Thus the α particle was calculated as two deuterons, a neutron and a helion, and as a proton and a triton. Their results include both possible relative angular momenta states of the two deuterons, L=0 and 2 , i.e. an S-state and a D-state in the α particle. For the ($\vec{d}$,α) transfer reaction, only the $< d\ d \mid \alpha >$ overlap was used, for reasons discussed in section 5.2 .

Schiavilla *et al.* calculated using two different nuclear interactions, the Argonne (AV14) and the Urbana (UV14). As discussed by Crosson *et al.*, the Argonne and Urbana interactions differ in three ways (Cro92a): (1) The AV14 one-pion-exchange-potential (OPEP) is 7% stronger than the UV14. (2) The UV14 potential has no short-range tensor interaction. (3) The parameters of the AV14 potential were determined using a more complete set of phase shifts then were those of UV14.

The TAP for the $^{50}Ti(\vec{d},\alpha)^{48}Sc$ reaction were calculated using the $< d\ d \mid \alpha >$ overlaps from these calculations as input for the distorted wave Born approximation (DWBA) calculations. Previous studies with transfer reactions (Mer87, Mer88) relied on phenomenological wave functions as these variational results were available as momentum-space functions only. The transformation of the $< d\ d \mid \alpha >$ overlaps into configuration space was accomplished by Crosson (Cro92a) making these realistic wave functions available for input to our DWBA calculations for the first time.

5.2 The $(\vec{d},\alpha)$ transfer reaction and the distorted-wave Born approximation

The α-particle wave function has a D-state configuration that is modeled as two deuterons with their spins aligned, S=2, with a relative orbital angular momentum of L=2 coupling to J=0. This configuration, represented in the $< d\ d \mid \alpha >$ overlap, can be probed using $(\vec{d},\alpha)$ transfer reactions.

The distorted wave Born approximation (DWBA) can be used to model direct transfer reactions (Sat83). In our model, the angular momentum considerations dictate picking up nucleons from the outermost shell of the target nucleus and the direct transfer of the nucleons as a deuteron cluster. The $(\vec{d},\alpha)$ differential cross sections peak at forward angles, which is characteristic of direct reactions at these energies.

When using a reaction to extract reliable information on either the projectile or the ejectile, one must ensure that the structure of the target nucleus and the reaction mechanism are both well-understood. The $(\vec{d},\alpha)$ reactions chosen for the project were selected because the transitions to stretched 7^+ final states in the daughter nuclei were expected to be pure L=6, J=7 transitions. In the shell-model picture, the target nucleus

A, here ^{50}Ti which has $J^{\pi}=0^{+}$, has its last neutron and proton, which are transferred during the reaction, in the $f_{7/2}$ shell. See figure 5.1. Contributions from the $g_{9/2}$ shell are expected to be small because that shell lies at a much higher energy. This pure L=6 transition removes ambiguities in the DWBA analysis which would be caused by L-mixing.

If the residual nucleus B, here ^{48}Sc, is left in a 7^{+} state then, by conservation of angular momentum, the angular momentum transfer, L_t, must be 6,7,or 8. The values for L-transfer, L_t = 7 and 8, can only be present if there is a D-state component in the α particle.

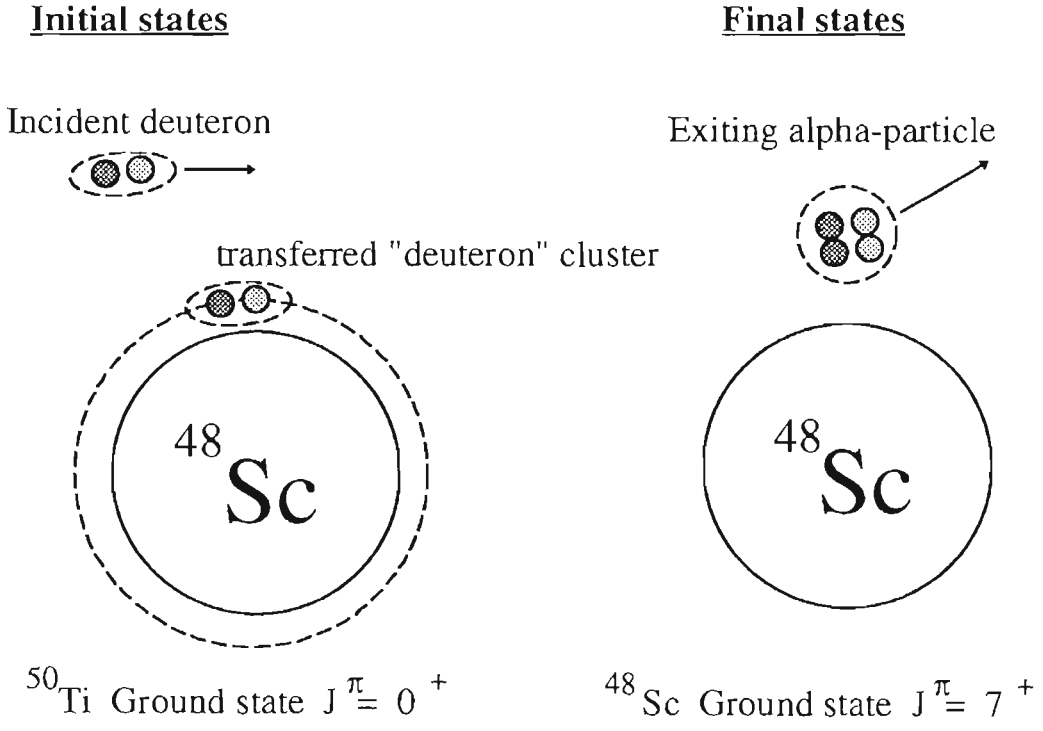

Figure 5.1 The ^{50}Ti(d,α)^{48}Sc transfer reaction schematic.

The DWBA transition amplitudes, written as,

$$T_{DWBA} = \int d\vec{r}_a \int d\vec{r}_b \; \chi_b^{*(-)} < J_B M_B \mid J_A M_A > < d\, d \mid V_{dd} \mid \alpha > \chi_a^{(+)} \qquad (5.1)$$

depend on the entrance channel wave functions χ_a, the exit channel wave functions χ_b, the $< d\, d \mid \alpha >$ overlap, the overlap of the target and residual nuclei $< J_B M_B \mid J_A M_A >$, and angular momentum coupling coefficients. The superscript (-) or (+) denotes the outgoing or incoming wave, respectively. The coupling coefficients are calculated in the computer code, TWOFNR (ToyPC) and the $< d\, d \mid \alpha >$ overlap integrals are directly input from numerical results of Fourier transforms of the variational results. The entrance channel wave functions were calculated using optical model parameters (OMP) from deuteron elastic scattering data taken at 16 MeV as discussed in section 5.4. The exit channel wave functions were calculated using OMP from α–particle elastic scattering data taken at 20 MeV as also discussed in section 5.4. The target nucleus was modeled with a Woods-Saxon potential as a ^{48}Sc core interacting with a neutron and proton bound as a deuteron cluster. The Woods-Saxon well-depth for the cluster-core interaction was chosen to reproduce the binding energy of a deuteron and ^{48}Sc core forming ^{50}Ti.

5.3 The ^{50}Ti($\vec{d}$,α)^{48}Sc Reaction to the $J^{\pi}=7^{+}$ State at E_X=1.096 MeV

The differential cross section, vector analyzing power, and two tensor analyzing powers, A_{xx} and A_{yy}, were measured at an incident deuteron energy of 16 MeV. The

polarized beam was produced using the TUNL Lamb-shift polarized ion source which was the precursor to the ABPIS source discussed in the preceding four chapters (Tra74). The data were taken with the beam switched between two spin states; one producing beam polarization P_{zz}= +0.7 and the other P_{zz} -1.4 using computer-controlled fast state change. The spin was flipped every run. Polarization axis rotations were performed by rotating the scattering chamber from a horizontal to a vertical position.

The beam polarization was measured continuously with a polarimeter designed and calibrated by Tonsfeldt (using the ^{3}He(d,p)^{4}He reaction), during the A_{yy} runs with the chamber in the horizontal orientation (Ton80). Beam polarizations were typically 70% of the theoretical maxima. The A_{xx} data were taken by rotating the chamber to the vertical position so that the spin was oriented in the reaction plane. Polarization measurements were taken at the start and at the finish of each sequence of A_{xx} data-taking. A sequence of runs, 2 spin-up and 2 spin-down, constituted each TAP measurement.

The deuteron beam impinged on the 260 $\mu g/cm^2$ titanium rolled foil. A slit feedback system was used to hold the beam in a fixed position on target. Eight solid-state silicon detectors 300 μm thick were set up at 10-degree intervals to take data at angles from 25 to 100 degrees. Solid angles varied from 0.8 to 1.3 msr; the larger solid angles were used at the back angle settings where the cross section is lower. By flipping the spin at the Lamb-shift polarized source we could take the data with all of the detectors on the same side of the scattering chamber. This data-taking scheme had been used previously to measure A_y and A_{yy} for the same reaction (Hal84). The second data set described here is more complete since the measurements were taken at more angles and A_{xx}, which is particularly sensitive to the α-particle D-state, was also measured.

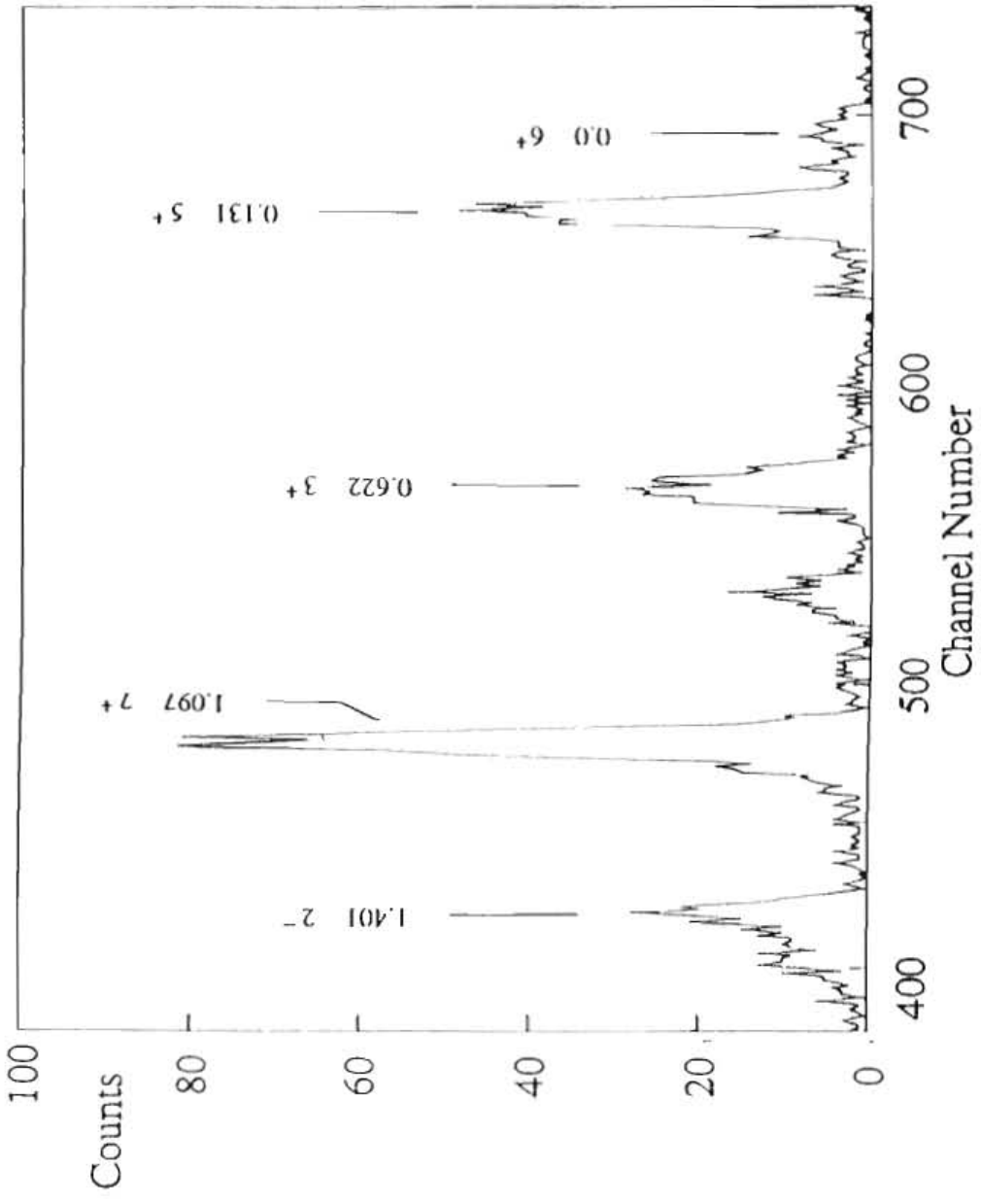

Figure 5.2 Spectra of the $^{50}Ti(d,\alpha)^{48}Sc$ reactions at $\theta=40^{o}$ with residual nucleus excitation energy from 0 to 1.6 MeV. Excitation energies are in MeV. The incident deuteron energy is 16 MeV.

A typical spectrum is shown in figure 5.2. The natural parity 2^+ state at 1.145 MeV could not be resolved in the spectra in spite of valiant efforts. The detectors had a full width at half-maximum (FWHM) of 27 keV, low enough to resolve the two peaks, but the straggling in the target and the noise on the signal could not be reduced enough. Thinner targets were fabricated using evaporation and sputtering techniques and electronic noise was reduced by shortening cables. At our best resolution of FWHM=37 keV, the count rate was much reduced and we could not see a distinct 2^+ peak. So we used the thicker target to increase the count rate; the FWHM for the data presented here is 56 keV.

The peak-fitting program SPECTR (Var86) was used in an attempt to extract the 2^+ and 7^+ yields, but that effort was unsuccessful. There was no evidence for a significant analyzing power in the shoulder that was presumably the 2^+ peak. Work done elsewhere show that the cross section for the 2^+ state is much smaller than that of the 7^+ state, which is the dominant peak in the spectrum (Gro67). The data presented here are not corrected, i.e., the 2^+ shoulder was included in the yield used to calculate the cross section and the TAP.

The error bars include statistical errors only. The statistical error in the polarization measurement was 2 to 3% and is not included in the error bars.

5.4 The OMP for the Entrance & Exit Channel Distorted Waves

Our early calculations of the $(\vec{d},\alpha)$ TAP using the DWBA code showed that the predictions for the $(\vec{d},\alpha)$ reaction observables at E_d=16 MeV are sensitive to the OMP

chosen. The deuteron OMP were not so critical, but we determined the optimum parameterization using our elastic scattering cross section and the vector analyzing power data. The final OMP obtained were very close to Daehnick's global parameter set values.

The α-particle OMP are much more critical. In order to satisfy the ansatz of the DWBA reaction model, the OMP must fit the elastic scattering data (Sat83). For alpha-particles, an OMP set must fit the elastic α-particle scattering data, lie in the correct discrete ambiguity for that elastic scattering, and also must work to calculate the cross section and vector analyzing power (VAP) for the $(\vec{d},\alpha)$ reaction. The DWBA calculations are quite sensitive to the α-particle OMP as will be discussed in section 5.5.

Table 5.1 The entrance channel OMP - the top row are the OMP used in the DWBA transfer reaction calculations and the bottom row are the OMP which gave the best fit to the ^{50}Ti (d,d) elastic scattering data.

V_o	r_o	a_o	W_D	r_D	a_D	W_{LS}	r_{LS}	a_{LS}
(MeV)	(fm)	(fm^{-1})	(MeV)	(fm)	(fm^{-1})	(MeV)	(fm)	(fm^{-1})
89.6	1.17	0.74	11.5	1.75	0.71	7.2	0.86	0.66
89.6	1.17	0.74	12.1	1.71	0.73	6.87	1.07	0.66

Table 5.2 The exit channel OMP - the top row are the OMP used in the DWBA transfer reaction calculations and the bottom row are the OMP which gave the best fit to the ^{48}Ti (α,α) elastic scattering data.

V_o	r_o	a_o	W_S	r_S	a_S
(MeV)	(fm)	(fm^{-1})	(MeV)	(fm)	(fm^{-1})
141.	1.26	0.71	11.5	1.75	0.71
170.	1.17	0.74	12.1	1.71	0.73

5.4.1 The Entrance Channel Optical Model Parameters

The deuteron elastic scattering data were taken at 16 MeV with the scattering chamber in the horizontal position. For these measurements, the polarization axis was rotated to be perpendicular to the reaction plane with the Wien filter rather than rotating the chamber. Four pairs of solid-state surface-barrier detectors were placed on the left and right sides of the scattering chamber at 10 degree angle intervals. We measured the cross section, the vector analyzing power, A_y, and the tensor analyzing power, A_{yy}, in five degree steps from 25 to 165 degrees.

Alpha-particles were stopped in aluminum foils placed in front of each detector. The deuteron elastic scattering peak was well-separated in the spectra. For the forward angles, 25 to 45 degrees, there was a neighboring ($\vec{d}$,d) elastic scattering peak from ^{48}Ti isotopic impurities in the target. These data were peakfit using the computer code SPECTR which fits Gaussian peak shapes to data. The channel numbers were set to values consistent with the kinematics and then the peak heights and widths were allowed to vary to achieve the best fit. The peak widths were consistent and there was no skew in the peaks.

The deuteron elastic scattering data were fit starting from Daehnick's global OMP set (Dae78). The only change was an slight increase in the spin-orbit real well depth. The cross section and vector analyzing power were both reproduced by the optical model calculation computed using the code OPTICS (Eas73), figure 5.2 .

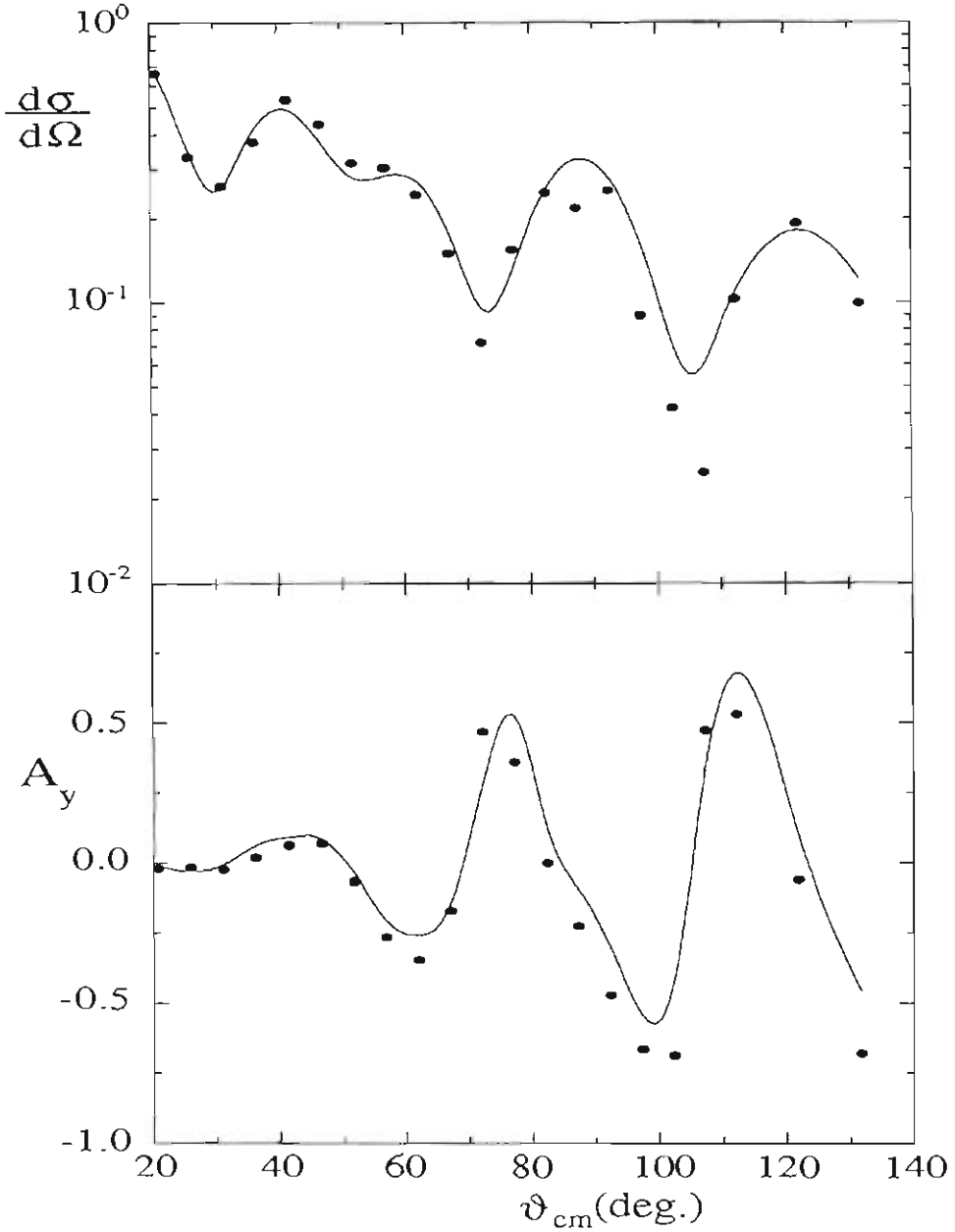

Figure 5.3 Angular distribution of the cross section divided by the Rutherford cross section and A_y, at E_d=16 MeV for $^{50}Ti(d,d)^{50}Ti$ elastic scattering. The curves are from an OPTICS calculation using the OMP described in the text.

5.4.2 The Exit Channel Optical Model Parameters

The α-particle elastic scattering data were taken at 20 MeV to match the energy of the exiting α-particles from the transfer reaction. The data were taken in five degree steps at angles from 25 to 165 degrees using four pairs of surface-barrier solid-state detectors in a symmetric left-right configuration in the scattering chamber. The residual nucleus in the $^{50}Ti(d,\alpha)^{48}Sc$ reaction is unstable so we used the $^{48}Ti(\alpha,\alpha)^{48}Ti$ reaction data to obtain exit channel OMP. These targets were made using direct ion sputtering (Cro93).

Finding the correct set of optical model parameters was much more difficult than for the deuteron scattering data. Alpha-particle scattering can be fit by many sets of optical model parameters; there are both discrete and continuous ambiguities in the possible parameter sets(Sat 83,Gol72). The rms radius and the volume integral, J_0 can be used to determine the most appropriate set of OMP. The OMP which best describe the elastic scattering must also provide an exit-channel wave function that reproduces the transfer-reaction data. The final

values used in the DWBA calculations are the result of a careful balance between preserving the best fit elastic scattering and a good fit to the cross section and vector analyzing power ($\vec{d}$,α) data from the DWBA calculation (See figure 5.3).

5.4.3 Trends in ($\vec{d}$,α) DWBA calculations - Exit Channel OMP

The underlying assumption in the DWBA is that the exit-channel particle scattering can be modeled using wave functions calculated from optical-model parameters that

reproduce the elastic-scattering data at the same energy. The alpha-particles, however, often exit the residual nucleus leaving it in an excited state, not the ground state.

To determine which set of OMP would fit the elastic scattering data and be a legitimate choice for the reaction, the cross section and vector analyzing power were calculated for the $(\vec{d},\alpha)$ reaction using just the S-state in the outgoing α-particle and compared to experimental values. Both σ and A_y are relatively insensitive (Cro 92a) to the α-particle D-state wave function. These calculations were performed in an iterative method, varying one parameter at a time in small steps and comparing the resulting observables.

The ratio of the α-particle real-well depth to imaginary-well depth mainly affected the cross section at back angles. If the imaginary potential is too low then the cross-section angular distribution remains relatively constant with angle, rather than dropping off, which is reasonable because the imaginary potential models the absorptive processes. The radii and diffuseness affect mostly the spacing of the maxima - which is just what you expect from hard-sphere scattering. The vector analyzing power moves up and down with the real-well depth, as if a constant offset were added. The VAP amplitude at back angles is determined by the imaginary-well depth; raising the absorption increases the amplitude.

Overall, the deuteron parameters affect the calculations the same way as the α-particle parameters but on a much smaller scale.

5.5 Results

The data and final DWBA calculations are shown in figure 5.4 . The α-particle S-state calculation is clearly inadequate to describe the data, especially A_{xx}, and there is a

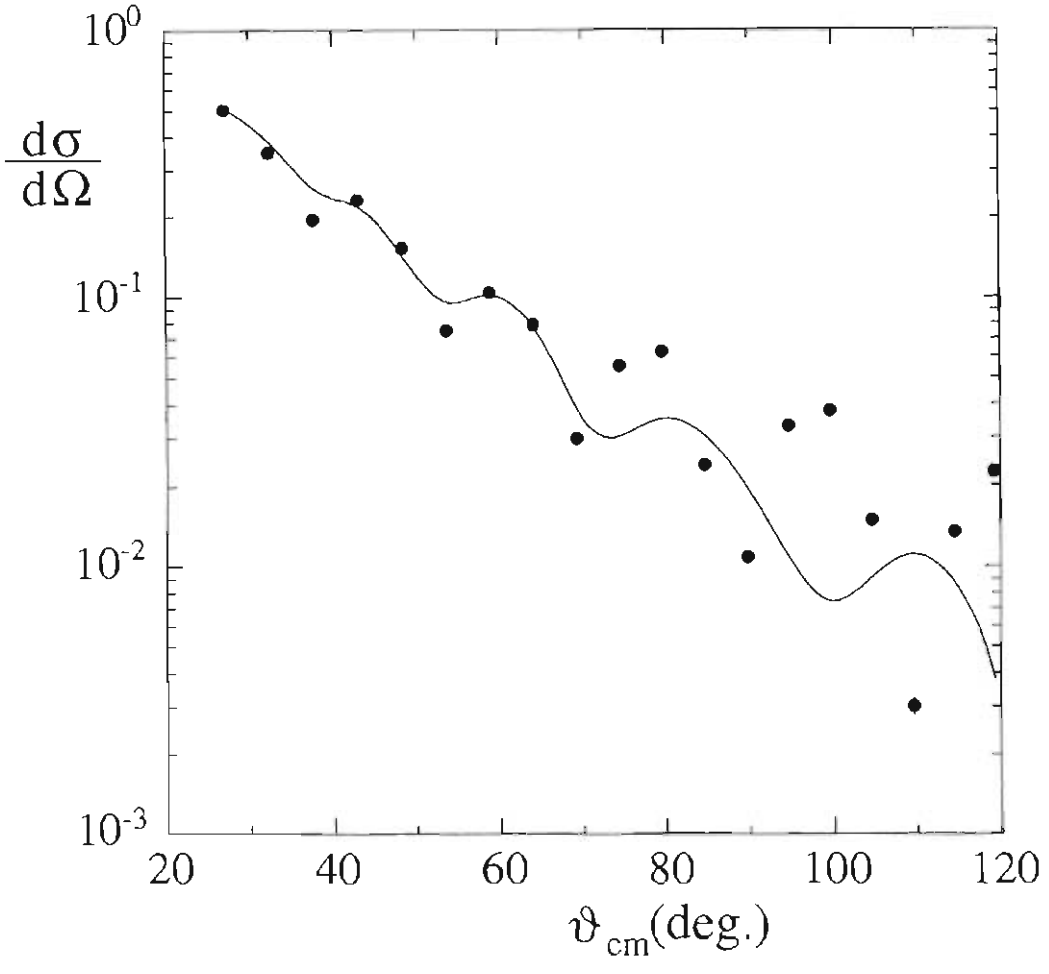

Figure 5.4 Angular distribution of the cross section divided by the Rutherford cross section, at E_α=20 MeV for $^{48}Ti(\alpha,\alpha)^{48}Ti$ elastic scattering. The curves are from OPTICS calculations using the OMP described in the text.

pronounced difference between the calculations for the two interactions used in the variational calculations. This single case of comparing $^{50}Ti(\vec{d},\alpha)^{48}Sc$ data with calculated observables is inadequate to judge the result of the method. A much stronger case is made when all the data from the project are examined (Cro93).

The greater sensitivity of A_{xx} as compared to A_{yy} to the α-particle D state can be understood from a semi-classical argument (Cro93). Simply put, the kinematics favor L_t=6 for this peripheral reaction, and the α-particle D state is more likely, at this energy, to be formed by a beam aligned along the x-axis than by a beam aligned along the y-axis.

As stated in section 5.1, there are generally problems with using DWBA for an analysis to extract ejectile information. The problems are caused by angular momentum mixing in the transition, ambiguities in the OMP versus the $< d\ d \mid a >$ form factor, and an unknown bound-state wave function for the target nucleus. Our choice of final states in a stretched configuration eliminates the possibility of angular momentum mixing. These $(\vec{d},\alpha)$ data, as well as the data from the other targets, ^{58}Ni and ^{48}Ti, were tested for sensitivity to the optical model parameters and the target bound-state parameters. Changes of 5% in the OMP caused marked effects in the cross section and VAP but left the TAP the same within 10%. The effects on A_{yy} were greater than on A_{xx}. The TAP observable, A_{yy} was not described well by the calculations.

5.6 Conclusions and Future Work

The α–particle D-state project as a whole was a success, the TAP were reproduced by the calculations and the calculations done with the realistic wave-functions (Cro92) showed sensitivity to the choice of NN interaction used. As for the $^{50}Ti(\vec{d},\alpha)^{48}Sc$ reaction in particular, the spectra used to extract the 7^+ information could be used to

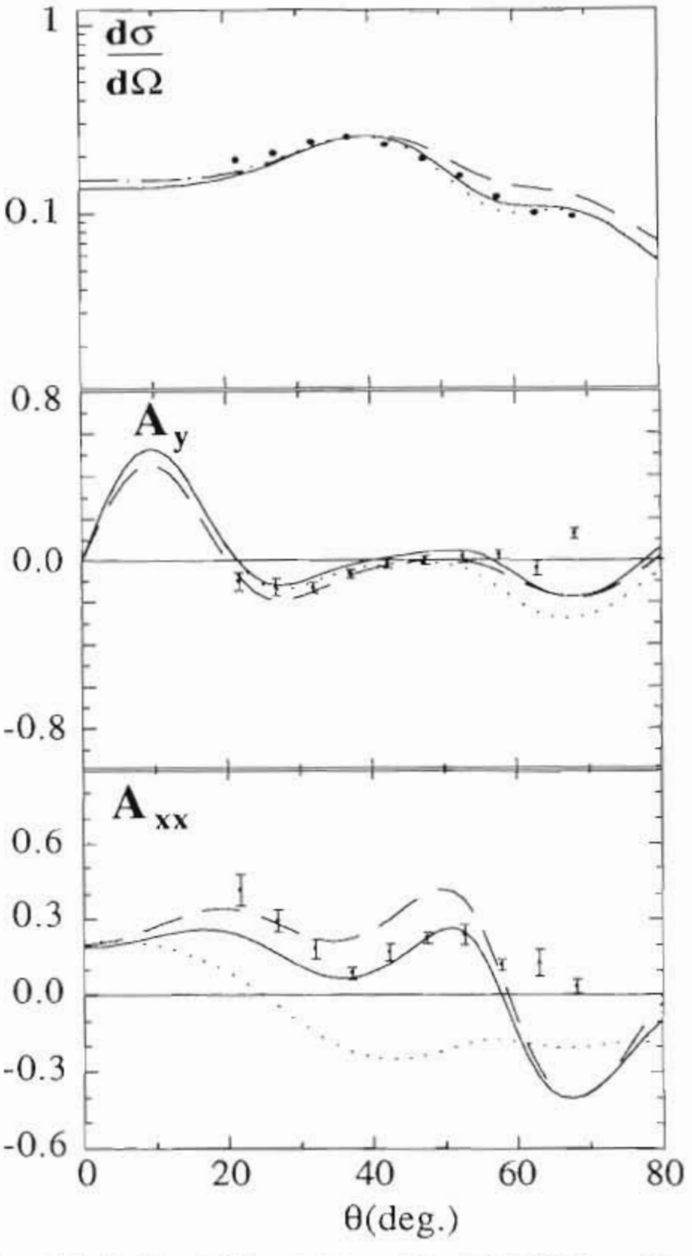

Figure 5.5 Angular distribution of the cross section ($d\sigma/d\Omega$) in mb/sr, A_y, and A_{xx}, at E_d=16 MeV for $^{50}Ti(d,\alpha)^{48}Sc$ to the 7^+ state in ^{48}Sc at E_x=1.097 MeV. The curves are DWBA calculations using realistic form factors for $< d\ d \mid \alpha >$ from the AV14 (solid lines) and UV14 (dashed lines) interactions. The dotted line corresponds to a pure S-state configuration for the d-d relative motion in the α particle. The DWBA calculation of $d\sigma/d\Omega$ is arbitrarily normalized to the data.

obtain L-mixing information now that the α-particle D-state effects are known. This work is in progress.

Two-step calculations done for ^{58}Ni($\vec{d}$,α)^{56}Co (Cro93) showed that two-step effects are negligible at 22 MeV and so the expectation is that two-step calculations are unnecessary for ^{50}Ti($\vec{d}$,α)^{48}Sc at 16 MeV.

The TUNL tandem accelerator has been upgraded to enable 20 MeV deuterons to be produced, so the data could be taken at a higher energy, closer to the 22 MeV used at Munich for the ^{58}Ni data (Cro 92a ,Cro 92c). At higher energies there should be fewer α-particle OMP ambiguities and the ^{50}Ti calculations might then compare as well to the data as do the ^{58}Ni data. That would lend even more credence to the work.

Appendix 1

Spin-filter Polarimeter Operation

This list should supply a user with the necessary details to connect the spin filter system used for this thesis research to its utilities and power supplies.

Oil cooling:

- The oil **must** enter the spin filter from the bottom and exit from the top.
- The oil pressure interlock switch must be connected to the oil interlock circuit.
- The oil interlock circuit must be connected to switch off the power supplies for the main coil and the two end coils in case there is a catastrophic problem with the oil pump or lines. **Never run with the interlocks disconnected.**
- Fill the oil lines at the pump under the tandem accelerator. Fill until the lines are bled.

-Magnets:

- When inserting the jig into the spin filter keep it on axis and level - if you bump the rf loops then the impedance match may change.
- All of the coils must have the same polarity and it must be the same as C3 on the ABPIS.
- The field should be flat to within 0.3 G over a 6" length inside the rf cavity. Check for final field uniformity after leaving the coils energized overnight.
- The inner coil field should ramp when connected to the Kepco bipolar supply and the field uniformity should not be affected by the inner coil.

-DC field:

- Use a voltmeter to check that there is +/- V on two opposite quadrants of the spin filter. Usually, one of two things is wrong if the voltage is not applied in the spin filter. The power supply potentiometers blow occasionally or the wires from the power supply at the feedthru on the spin filter can become disconnected.

The rf field:

- Use the Bird meter to check that there is from 0 - 250 mW of forward power to the cavity. The reverse power should be less than 5 mW for 60 mW forward power.
- Changing the drive loop cable may improve the match.

Photomultiplier tube:

- The PMT should only be biased negatively.
- Use the deuterium lamp to check that there is a signal from the tube.
- Check the gain versus photomultiplier tube voltage, it should match the specifications.
- Check the batteries for the Ithaco pre-amplifier.

Quench plate:

- Check that the quench plate is electrically isolated and that the voltage is applied.
- The following is a list of the spin filter polarimeter parameters which were successful for normal operation during the ABPIS spin-filter polarimeter runs.

Spin Filter parameters:

DC voltage = 85 V

rf forward power = 600 mW

Main coil pot = 2.85 on Coarse, 4.86 on Fine, Centered on State 2

The states appeared at 4.56, 4.87, 5.18 on the Fine pot.

Trim coil pots: Upstream Trim = 3.03, Downstream Trim = 3.55

End coil pots: Upstream End = 8.50, Downstream end = 9.70

Inner coil ramped from roughly 520-620 G.

Quench plate voltage = 800 V.

Phototube voltage = -1100 V to -1500 V

Make sure that the Ithaco pre-amp is on the low-noise setting and that it does not overload.

ABPIS: (except when testing variation in these parameteres)

Ionizer at +550 or +1100 V

Lens 1 = 0

Lens 2 = +190 V

Lens 3 = +200 V

Lens 4 = 0 = Lens 5 = Lens 6 = Lens 7

All resistors on acceleration tube were grounded at each end.

The peak in metastable beam production occurs at a Cs oven temperature of 194 C.

Appendix 2

Tables of Measurements for $^{50}Ti(\vec{d},\alpha)^{48}Sc$ Reaction Observables

Table A.1 Compiled below are the center-of-mass cross section, $d\sigma/d\Omega$, vector analyzing power, A_y, and two tensor analyzing powers, A_{xx} and A_{yy} measurements for the $^{50}Ti(\vec{d},\alpha)^{48}Sc$ reactions taken at the Triangle Universities Nuclear Laboratory at an incident deuteron beam energy of 16 MeV.

Lab Ang.	A_y	A_y error	A_{yy}	A_{yy} error	A_{xx}	A_{xx} error	$d\sigma/d\Omega$ (mb/sr)	$d\sigma/d\Omega$ error
22.	-0.100	0.041	0.152	0.058	0.413	0.060	192.	0.547
25.	-0.126	0.041	0.172	0.053	0.294	0.043		
27.	-0.171	0.036	0.118	0.047	0.304	0.042	208.	0.506
30.	-0.129	0.026	0.039	0.037	0.186	0.039	239.	0.426
35.	-0.049	0.037	-0.040	0.053	0.089	0.037	254.	0.306
40.	-0.018	0.022	-0.106	0.032	0.172	0.032	230.	0.260
45.	-0.006	0.019	-0.026	0.053	0.220	0.038	194.	0.242
50.	0.000	0.026	-0.250	0.040	0.241	0.038	158.	0.232
55.	0.024	0.021	-0.167	0.048	0.136	0.034	121.	0.266
60.	-0.039	0.034	-0.301	0.053	0.130	0.040	100.	0.227
65.	0.128	0.025	-0.146	0.055	0.030	0.028	96.	0.179

Table A.2- Measured cross section and vector analyzing power for the $^{50}Ti(\vec{d},d)^{50}Ti$ elastic scattering at an incident deuteron energy of 16 MeV are in the left columns. Measured cross section for $^{48}Ti(\alpha,\alpha)^{48}Ti$ elastic scattering at an incident alpha- particle energy of 20 MeV are in the right columns

Lab Ang.	A_y	A_y error	$d\sigma/d\Omega$ (mb/sr)	$d\sigma/d\Omega$ error	Lab Ang.	$d\sigma/d\Omega$ (mb/sr)	$d\sigma/d\Omega$ error
25.	-0.021	0.001	1775.	45.46	25.	1362.1	3.178
30.	-0.015	0.002	353.1	21.13	30.	452.2	1.006
35	-0.025	0.003	133.9	12.92	35.	138.7	4.549
40.	0.019	0.003	106.3	10.78	40.	98.52	0.387
45.	0.064	0.004	89.52	10.57	45.	41.83	1.661
50.	0.070	0.005	46.97	7.378	50.	13.94	0.147
55.	-0.069	0.006	23.06	5.279	55.	13.75	0.268
60.	-0.266	0.010	15.66	4.226	60.	7.661	0.110
65.	-0.346	0.013	9.230	4.226	65.	2.189	0.034
70.	-0.171	0.013	4.247	2.227	70.	3.167	0.038
75.	0.470	0.016	1.581	1.276	75.	2.861	0.170
80.	0.359	0.015	2.706	1.756	80.	0.887	0.012
85.	0.000	0.008	3.501	1.872	85.	0.335	0.006
90.	-0.226	0.010	2.543	1.366	90.	0.870	0.056
95.	-0.472	0.015	2.464	1.572	95.	0.843	0.102
100.	-0.665	0.019	0.750	0.753	100.	0.292	0.005
105.	-0.688	0.021	0.303	0.575	105.	0.052	0.003
110.	0.473	0.030	0.156	0.348	110.	0.206	0.005
115.	0.530	0.021	0.574	0.780	115.	0.310	0.009
120.	-0.060	0.024	0.872	1.293			
125.	-0.681	0.037	0.380	0.801			

References

Chapter 1-4: Spin-filter polarimeter reference list

(Bel87) A.S. Belov, S.K. Yesin, S.A. Kubalov, V.E. Kuzik, A.A. Stepanov, and Y.P. Yakushev, Nucl. Instrum. Meth. **A255** (1987) 442.

(Bla93) T.C. Black *et al.*, to be published in Nucl. Instr. Meth.

(Bre31) G. Breit & I.I. Rabi, Phys. Rev. **38** (1931) 2082

(Buc91) L. Buchmann, Nucl. Instr. Meth. **A301** (1991) 383.

(Bro71) J.E. Brolley *et al.*, Proc. Third Int. Symp. on Polarization Phenomena in Nuclear Reactions, Madison, 1970, eds. H.H. Barschall and W. Haeberli (Univ. Wisconsin Press, 1971) 846.

(Cla67) G. Clausnitzer & D. Fick, Nucl. Inst. Meth. **47** (1967) 171.

(Cle74) T.B. Clegg *et al.*, Nucl. Instr. Meth. **120** (1974) 445.

(Cle82) T.B. Clegg , Proc. Conf. on Polarized Proton Sources, Ann Arbor 1981, eds. A.D. Krisch and A.T.M. Lin, Am. INst. Phys. Conf. **80** (1982) 21.

(Cle84) T.B. Clegg *et al.*, AIP Conference Proc. **117** (1984) 63.

(Cle88) T.B. Clegg *et al.*, Proc. Int. Symp. on Polarization Phenomena in Nuclear Reactions, Paris 1989.

(Cle93) T.B. Clegg *et al.*, , in preparation.

(Cro91) E.R. Crosson, T.B. Clegg, H.J. Karwowski, and S.K. Lemieux, Nucl. Instrum. Meth. **A310** (1992) 703.

(CroPC) E.R. Crosson, private communication (1992)

(Din93) D.C. Dinge *et al.*, in preparation.

(Dri80) L.J. Dries *et al.*, Phys. Rev. **C21**, 475 (1980).

(Fle93) K.A. Fletcher *et al.*, to be published in Nucl. Instr. Meth.

(Hae67) W. Haeberli, Ann. Rev. Nucl. Sci. **17** (1967) 373.

(Ham91 Hamamatsu Technical Data No. S-505-03.

(Heb60) J. Heberle, Helv. Phys. Acta Suppl. **6** (1960) 140.

(Lem93) S.K. Lemieux, E.R. Crosson, H.J. Karwowski, & T.B. Clegg, to be published in Nucl. Instr. Meth.

(Leo87) W.R. Leo, Techniques for Nuclear and Particle Physics Expts., pub. Springer-Verlag Berlin Heidelberg (1987) 169-190.

(Lis76) P.W. Lisowski *et al.* , Phys. Rev. Lett. **20** (1976) 809.

(McK77) J.K. McKibben, Am. Jour, Phys. **45** (1977) 1022.

(Mot36) L. Motz & M.E. Rose, Phys. Rev. **50** (1936) 348

(Ohl67) G.G. Ohlsen and J.L. McKibben, "Theory of a radio-frequency 'spin filter' for a metastable hydrogen, deuterium, or tritium atomic beam", Los Alamos Scientific Laboratory Report, LA-3725 (1967).

(Ohl69-1) G.G. Ohlsen, J.A. Jackson, J.L. McKibben, and G.P. Lawrence, "Design of a solenoid for a Lamb-shift polarized ion source", Los Alamos Scientific Laboratory Report LA-4082 (1969).

(Ohl69-2) G.G. Ohlsen, J.L. McKibben, R.R. Stevens, G.P. Lawrence, and N.A. Lindsay, "Operation of a radio-frequency nuclear spin filter", Los Alamos Scientific Laboratory Report LA-4112 (1969).

(Pli76) Yu.A. Pliss & L.M. Soroko, Nucl. Instr. Meth. **135** (1976) 497.

(Pri93) J.S. Price and W. Haeberli, Nucl. Instr. Meth. **A326** (1993) 416.

(Sak85) A.K. Sakurai, Modern Quantum Mechanics, pub. McGraw-Hill (1985).

(Sch87) P. Schiemez, Helv. Phys. Acta **59** (1987) 620-627.

(Tag92) Y. Tagishi, N. Nakamoto, K. Katoh, J. Togawa, T. Hisamune, and T. Yoshida, Phys. Rev. **C46** (1992) R1155.

(Tho93) W.J. Thompson, to be published in Nucl. Instr. Meth.

(Tra74) T. Trainor, Ph.D. dissertation, University of North Carolina, 1974, (unpublished), available from University Microfilms International, 300 N. Zeeb Rd., Ann Arbor, Michigan 48106.

(Wiz79) J.L. Wiza, Nucl. Instr. Meth. **162** (1979) 587-601.

(Yna87) K. Ynamamoto *et al.*, Nucl. Instr. Meth. **A253** (1987) 542-547.

Chapter 5: A study of the α-particle D-state reference list

(Cro92a) E.R. Crosson, Ph. D. dissertation, University of North Carolina, 1992, (unpublished), available from University Microfilms International, 300 N. Zeeb Rd., Ann Arbor, Michigan 48106.

(Cro92b) E.R. Crosson, *et al.*, Phys. Rev. **C45**, (1992) 492.

(Cro93) E.R. Crosson, *et al.*, (1993) Accepted for publication Phys. Rev.

(Eas73) R.J. Eastgate, W.J. Thompson, and R.A. Hardekoph, Comp. Phys. Comm. **5** (1973) 69

(Gol72) D. A. Goldberg and S. M. Smith, Phys. Rev. Lett. **29**, 500 (1972); D. A. Goldberg, S.M. Smith and G.F. Burdzik, Phys. Rev. **C10**, 1362 (1974).

(Gro67) K. Grotowski, S. Wiktor, and F. Pellegrini, Nuo. Cim. **47B** (1967) 255

(Hal84) M. Haller *et al.*, Nucl. Phys. **A 419** (1984) 45.

(Mer87) F. Merz *et al.*, Phys. Lett. **B 183** (1987) 144.

(Mer88) F. Merz *et al.*, Nucl. Phys. **A 489** (1988) 399.

(Pla75) G. R. Plattner, R.D. Viollier, K. Alder, Phys. Rev. Lett. **34** (1975) 830.

(San84) F.D. Santos, A.M. Eiro, Portgal. Phys. 15 (1984) 65.

(Sat83) G. R. Satchler, *Direct Nuclear Reactions*, Oxford University Press, New York, 1983.

(Sch42) J. Schwinger, Phys. Rev. **61** (1942) 138.

(Sch86) R. Schiavilla, V.R. Pandharipande, R.B. Wiringa, Nucl. Phys. **A449** (1986) 219.

(Ton80) S.A. Tonsfeldt, Ph. D. dissertation, University of North Carolina, 1980, (unpublished), available from University Microfilms International, 300 N. Zeeb Rd., Ann Arbor, Michigan 48106.

(Tra74)) T.A. Trainor, T.B. Clegg, and P.W. Lisowski, Nucl. Phys. **24** (1974) 533.

(Var86) R.L. Varner, Ph. D. dissertation, University of North Carolina, 1986, (unpublished), available from University Microfilms International, 300 N. Zeeb Rd., Ann Arbor, Michigan 48106.